

New *XMM-Newton* observations of faint, evolved supernova remnants in the Large Magellanic Cloud[★]

P. J. Kavanagh,^{1†} M. Sasaki,² M. D. Filipović,³ S. D. Points,⁴ L. M. Bozzetto,³ F. Haberl,⁶
P. Maggi,⁵ C. Maitra⁶

¹*School of Cosmic Physics, Dublin Institute for Advanced Studies, 31 Fitzwilliam Place, Dublin 2, Ireland*

²*Dr Karl Remeis Observatory and ECAP, Friedrich-Alexander-Universität Erlangen-Nürnberg, Sternwartstr. 7, 96049 Bamberg, Germany*

³*Western Sydney University, Locked Bag 1797, Penrith South DC, NSW 2751, Australia*

⁴*NSF's NOIRLab/CTIO, Casilla 603, La Serena, Chile*

⁵*Université de Strasbourg, CNRS, Observatoire astronomique de Strasbourg, UMR 7550, F-67000 Strasbourg, France*

⁶*Max-Planck-Institut für extraterrestrische Physik, Gießenbachstraße 1, D-85748 Garching, Germany*

Accepted 2022 March 13. Received 2022 February 25; in original form 2021 November 1

ABSTRACT

The Large Magellanic Cloud (LMC) hosts a rich population of supernova remnants (SNRs), our knowledge of which is the most complete of any galaxy. However, there remain many candidate SNRs, identified through optical and radio observations where additional X-ray data can confirm their SNR nature and provide details on their physical properties. In this paper, we present *XMM-Newton* observations that provide the first deep X-ray coverage of ten objects, comprising eight candidates and two previously confirmed SNRs. We perform multi-frequency studies using additional data from the Magellanic Cloud Emission Line Survey (MCELS) to investigate their broadband emission and used *Spitzer* data to understand the environment in which the objects are evolving. We confirm seven of the eight candidates as *bona-fide* SNRs. We used a multi-frequency morphological study to determine the position and size of the remnants. We identify two new members of the class of evolved Fe-rich remnants in the Magellanic Clouds (MCs), several SNRs well into their Sedov-phase, one SNR likely projected towards a HII region, and a faint, evolved SNR with a hard X-ray core which could indicate a pulsar wind nebula. Overall, the seven newly confirmed SNRs represent a $\sim 10\%$ increase in the number of LMC remnants, bringing the total number to 71, and provide further insight into the fainter population of X-ray SNRs.

Key words: ISM:supernova remnants - Magellanic Clouds - X-rays: ISM

1 INTRODUCTION

Supernova remnants (SNRs) are the objects that result from the interaction of ejecta from supernova (SN) explosions with the surrounding medium. These types of explosions are generally divided into two categories: the core-collapse of a massive star, or the explosion of a carbon-oxygen white dwarf in a binary system which has exceeded the Chandrasekhar limit due to accretion or merger. SNe and their SNRs are critical engines of the matter cycle in galaxies. They power the mechanical evolution of the interstellar medium (ISM), they seed the ISM with heavy elements which are available for future generations of star-formation, and they are prodigious producers of cosmic rays (for a review see Vink 2012; Filipović & Tothill 2021a). Therefore, by understanding their physics and evolution we will better understand the matter cycle in galaxies. Studies of evolved SNRs in the Galaxy are difficult because of uncertain distance estimates and high foreground absorption, which effectively

shields the emission from their low temperature plasmas from our view. Therefore, to perform unbiased studies of evolved SNRs we must look to nearby galaxies.

The Large Magellanic Cloud (LMC) is perfectly suited for the study of evolved SNRs. It is located at a distance of 50.0 ± 1.3 kpc (Pietrzyński et al. 2013), is oriented almost face-on (inclination angle of $30\text{--}40^\circ$, van der Marel & Cioni 2001; Nikolaev et al. 2004), and its location outside of the Galactic disk means it is subject to relatively low line-of-sight absorption (average Galactic foreground $N_{\text{H}} \approx 7 \times 10^{20} \text{ cm}^{-2}$) making evolved SNRs more easily observable. Prior to this work there were 64 confirmed SNRs in the LMC and many more candidates (Yew et al. 2021; Maitra et al. 2021; Filipović et al. 2022, and references therein), and we have performed an extensive study of the known population in X-rays (Maggi et al. 2016) and radio (Bozzetto et al. 2017).

Our SNR candidate sample in recent years was identified based on *ROSAT* data, in particular from the study of Haberl & Pietsch (1999). Many of these objects were confirmed as evolved SNRs using follow-up *XMM-Newton* observations or data from the Very Large Programme (VLP) survey of the LMC (PI: Frank Haberl), along with radio observations, e.g., Bozzetto et al. (2014), Maggi et al. (2014), Kavanagh et al. (2015a), Kavanagh et al. (2015b), Ka-

[★] Based on observations obtained with *XMM-Newton*, an ESA science mission with instruments and contributions directly funded by ESA Member States and NASA

† E-mail: pkavanagh@cp.dias.ie

vanagh et al. (2016). In this paper we present *XMM-Newton* observations to SNR candidates identified with either *ROSAT* in Haberl & Pietsch (1999) or in the radio continuum in Bozzetto et al. (2017), supplemented by optical emission line data from the Magellanic Cloud Emission Line Survey (MCELS, Smith et al. 2006).

In this and our previous works, we adopt the criteria of the Magellanic Cloud Supernova Remnant (MCSNR) Database for SNR classification, i.e. a candidate must meet at least two of the following three criteria to be confirmed as an SNR: significant $H\alpha$, $[S\ II]$, and/or $[O\ III]$ line emission with an $[S\ II]/H\alpha > 0.4$ (Mathewson & Clarke 1973; Fesen et al. 1985; Filipovic et al. 1998; Filipović & Tothill 2021b); extended non-thermal radio emission, typically with spectral index $\alpha \approx -0.5$ ¹ for an evolved remnant; and/or soft thermal X-ray emission. As shown in the forthcoming text, seven of our eight candidates were confirmed as SNRs based on their radio, optical, and/or X-ray properties conforming to the MCSNR classification scheme. Therefore, to avoid confusion, we will hereafter refer to these objects using their MCSNR identifier. These are given in Table 1 and their locations within the LMC are shown in Fig. 1.

Our paper is arranged as follows: the observations and data reduction are described in Sect. 2, data analysis is outlined in Sect. 3, results are given in Sect. 4, we discuss our results in Sect. 5, and finally we summarise our work in Sect. 6.

2 OBSERVATIONS AND DATA REDUCTION

2.1 X-ray

Each of our candidates was observed with *XMM-Newton* (Jansen et al. 2001) with the European Photon Imaging Camera (EPIC) as the primary instrument. The EPIC comprises a pn CCD (Strüder et al. 2001) and two MOS CCD (Turner et al. 2001) imaging spectrometers. All the observational data were reduced using the standard reduction tasks of SAS² version 18.0.0. The details of each observation are given in Table 2 which also lists each of the exposure times after filtering for periods of high particle background. We note that MCSNR J0512–6717 was observed serendipitously by *XMM-Newton* on May 2014 (Obs. ID 0741800201, PI P. Kavanagh) during an observation of the nearby remnant MCSNR J0512–6707 ([HP99] 483). Further details on these observations can be found in Kavanagh et al. (2015c).

¹ Defined by $S \propto \nu^\alpha$, where S is flux density, ν is the frequency and α is the spectral index.

² Science Analysis Software, see <http://xmm.esac.esa.int/sas/>

Table 1. MCSNR identifiers for the confirmed SNRs in our sample.

Candidate name	Reference ^(a)	MCSNR Id.
0447–6918	B	MCSNR J0447–6919
[HP99] 460	H, M ^(b)	MCSNR J0448–6700
0449–6903	B	MCSNR J0449–6903
0456–6951	B	MCSNR J0456–6950
[HP99] 529	H	MCSNR J0504–6723
0510–6708	B	MCSNR J0510–6708
0512–6717	B	MCSNR J0512–6717
0527–7134	B	MCSNR J0527–7134
0542–7104	Y ^(b)	MCSNR J0542–7104

Notes: ^(a) B: Bozzetto et al. (2017), H: Haberl & Pietsch (1999), M: Maggii et al. (2016), Y: Yew et al. (2021). ^(b) Previously confirmed as SNR.

2.2 Optical

To search for optical emission signatures of SNRs we made use of both imaging and, in one case, spectroscopic observations.

2.2.1 Imaging

We used the MCELS (Smith et al. 2006) for our imaging analysis. The observations were taken with the 0.6 m University of Michigan/Cerro Tololo Inter-American Observatory (CTIO) Curtis Schmidt Telescope producing individual images of $1.35^\circ \times 1.35^\circ$ at a scale of $2.3'' \text{ pixel}^{-1}$ in narrow bands covering $[O\ III]\lambda 5007\text{\AA}$, $H\alpha$, and $[S\ II]\lambda 6716, 6731\text{\AA}$, along with matched green and red continuum bands. These individual images were flux calibrated and combined to create the final Magellanic Cloud mosaics. We extracted cutouts from the LMC mosaic centred on each of our objects. We then subtracted the appropriate continuum images from the emission line images to remove stellar continuum and reveal the full extent of the faintest diffuse emission. Finally, we produced $[S\ II]/H\alpha$ maps for each of our objects by dividing the continuum-subtracted $[S\ II]$ image by the continuum-subtracted $H\alpha$ image. The emission line images and contours derived from the $[S\ II]/H\alpha$ maps for each remnant are shown in the top-right of Figs. 2–11.

2.2.2 MCSNR J0512–6717 spectroscopy

The $[S\ II]/H\alpha$ map determined from the MCELS images of MCSNR J0512–6717 revealed sporadic regions $[S\ II]/H\alpha \gtrsim 0.4$ that were not coincident with the X-ray SNR shell. Therefore, we identified two $H\alpha$ and $[S\ II]$ bright filaments with $[S\ II]/H\alpha \gtrsim 0.4$ which were located in the X-ray shell (see Fig. 9 top-right) and performed follow-up observations using the Wide-Field Spectrograph (WiFeS, Dopita et al. 2007, 2010) integral field unit (IFU) mounted on the Australian National University 2.3 m Telescope at the Siding Springs Observatory. WiFeS provides optical spectra in a $25'' \times 38''$ field of view in the 3300–9200 Å range. This field is divided into twenty-five $1''$ wide slitlets with $0.5''$ sampling along the $38''$ lengths. We used the R3000 and B3000 dispersers for the red and blue cameras, respectively, to achieve a spectral resolution of $R=3000$ across the wavelength range. Both fields in MCSNR J0512–6717 were observed on 2015-10-09 (Prop. ID: 3150070). Field 1 (RA=05:12:48.8, Dec=−67:16:29) was observed for 180 s and field 2 (RA=05:12:27.8, Dec=−67:18:32) for 120 s. We reduced the raw data using the PyWiFeS³ data reduction pipeline (Childress et al. 2014).

2.3 Infrared

To aid in the discussion of the multi-wavelength morphology of our objects, we made use of data from the SAGE survey of the LMC (Meixner et al. 2006) with the *Spitzer Space Telescope* (Werner et al. 2004). The SAGE data set comprises a 7×7 degree survey of the LMC with the Infrared Array Camera (IRAC, Fazio et al. 2004) in the $3.6\ \mu\text{m}$, $4.5\ \mu\text{m}$, $5.8\ \mu\text{m}$, and $8\ \mu\text{m}$ bands, and with the Multiband Imaging Photometer (MIPS, Rieke et al. 2004) in the $24\ \mu\text{m}$, $70\ \mu\text{m}$, and $160\ \mu\text{m}$ bands. For this work we extracted cutouts from the MIPS $24\ \mu\text{m}$ mosaic for each of our objects using the NASA/IPAC Infrared Science Archive⁴ tools, which are shown in the bottom right

³ Available from <http://www.mso.anu.edu.au/pywifes/doku.php>

⁴ See <http://irsa.ipac.caltech.edu/data/SPITZER/SAGE/>

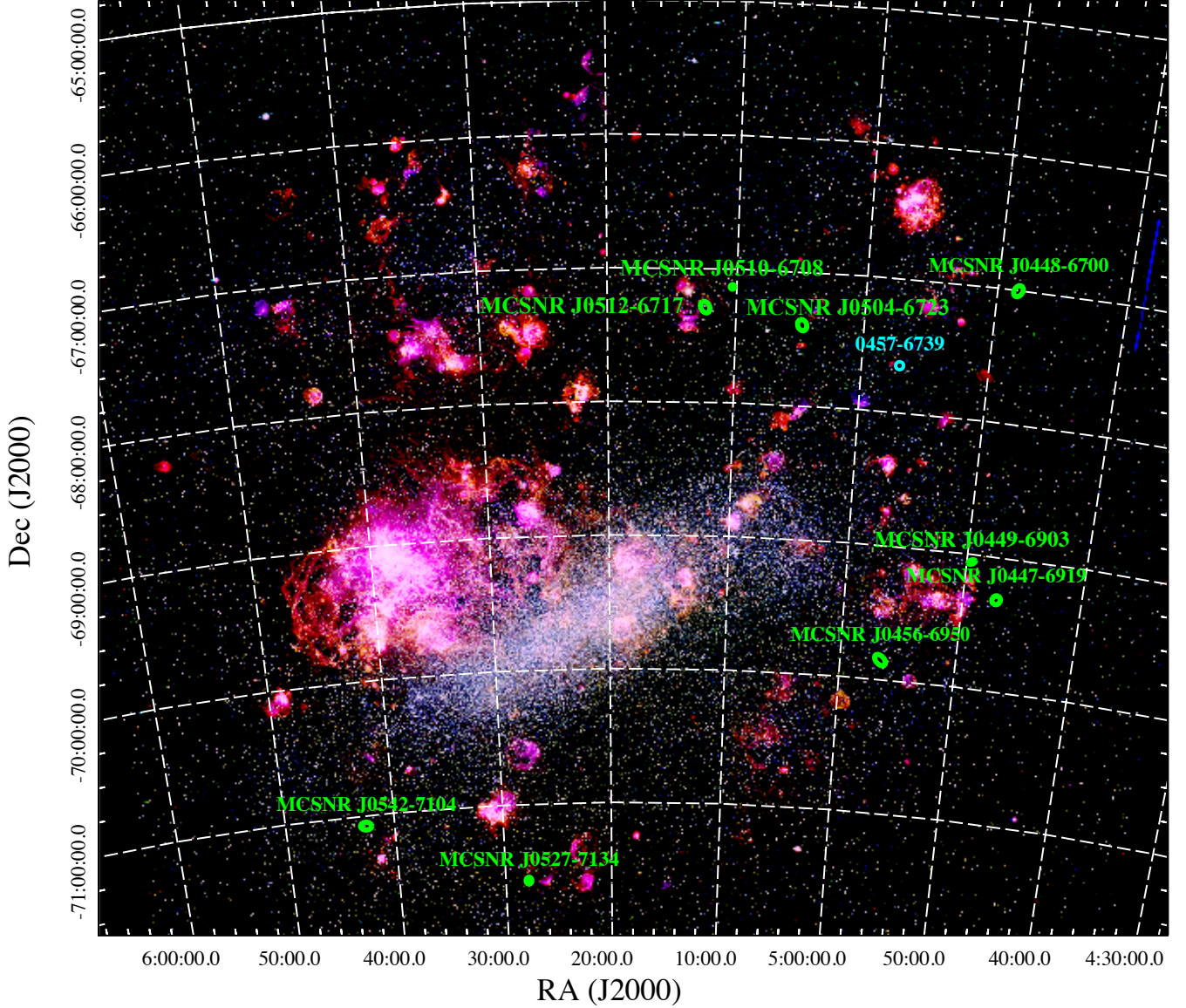


Figure 1. The location of our SNR sample plotted on a three-colour MCELS mosaic of the LMC (RGB = $H\alpha$, [S II], [O III]). All confirmed SNRs are shown in green. The unconfirmed candidate 0457–6739 is shown in cyan.

Table 2. XMM-Newton observations of LMC SNRs and candidates. The listed exposure times are flare-filtered. The PI for all observations was P. Kavanagh.

Target	Obs. ID	Date	RA (J2000)	Dec (J2000)	Exp. time (ks)		
					pn	MOS1	MOS2
[HP99] 483	0741800201	2014-05-17	05:12:28.0	-67:07:27	42.1	48.2	45.9
[HP99] 460	0764060101	2015-06-20	04:48:22.5	-67:00:04	27.6	32.3	32.3
[HP99] 529	0764060201	2015-08-19	05:04:49.5	-67:24:15	26.7	31.2	31.3
0527-7134	0780620101	2016-10-16	05:27:48.5	-71:34:06	18.6	31.3	29.3
0457-6739	0801990201	2017-10-27	04:57:33.0	-67:39:06	16.6	43.2	42.8
0449-6903	0801990401	2017-10-26	04:49:34.0	-69:03:34	3.0	12.0	12.3
0447-6918	0801990301	2017-09-28	04:47:09.7	-69:18:58	17.8	37.1	35.9
0456-6950	0841660501	2019-10-08	04:56:30.3	-69:50:47	31.1	45.6	45.6
0449-6903	0841660101	2019-10-15	04:49:34.0	-69:03:33	34.7	52.5	52.5
0510-6708	0841660401	2020-04-07	05:10:11.4	-67:08:03	28.4	39.8	39.2
0542-7104	0841660201	2020-04-19	05:42:45.0	-71:04:00	28.6	42.4	41.9

panels of Figs. 2–11. These images reveal the stochastically, thermally, and radiatively heated dust in the vicinity of our objects at a comparable resolution to *XMM-Newton*.

3 ANALYSIS

3.1 X-ray imaging

We produced particle background subtracted, exposure corrected, and adaptively smoothed EPIC images in three energy bands particularly suited to the analysis of SNRs: a soft band from 0.3–0.7 keV that includes strong lines from O; a medium band from 0.7–1.1 keV which contains Fe L-shell lines as well as Ne He α and Ly α lines; and a hard band (1.1–4.2 keV) that includes lines from Mg, Si, S, Ca, Ar, as well as non-thermal continuum if present. To produce these images, we followed the same procedure outlined in detail in many of our previous works, e.g. Kavanagh et al. (2015b,c, 2016); Maggi et al. (2016). A three-colour image of each of our objects was created, and are shown in the top left panels of Figs. 2–11.

3.2 X-ray point sources

Point sources located within the extent of our objects may be associated with and provide evidence of the nature of the SN progenitor of our objects. For example, the identification of a remnant compact object suggests an SNR resulted from a core-collapse event. To search for point sources, we extracted images from each of the EPIC instruments in the standard energy bands 0.2–0.5 keV, 0.5–1 keV, 1–2 keV, 2–4.5 keV, and 4.5–12 keV to use as input to the SAS task `edetect_chain`. For an adopted minimum-detection likelihood⁵ of 10, we detected several sources potentially associated with our objects. These sources were visually inspected and many that were identified as false sources due to structure in the extended emission of our objects were excluded. Detailed analysis of the remaining sources, including the identification of counterparts, is deferred to Appendix A. None of our detected point sources could be confirmed as the remnant compact objects of the SN explosions.

3.3 X-ray spectral analysis

Before extracting spectra we generated vignetting-weighted event lists for each EPIC instrument to correct for the effective area variation across FOV using the SAS task `evigweight`. We extracted source and background spectra from these corrected event lists with the source spectra extracted from elliptical regions encompassing the extended emission from our objects and the background spectra from a larger annular regions. Detected point sources were excluded in each case. To allow the use of the χ^2 statistic in the spectral fitting process, all spectra were rebinned so that each bin contained a minimum of 30 counts. We fitted the EPIC-pn and EPIC-MOS source and background spectra simultaneously in XSPEC (Arnaud 1996) version 12.11.1 with abundance tables set to those of Wilms et al. (2000, hereafter W00), the photoelectric absorption cross-sections of Balucinska-Church & McCammon (1992), and atomic data from ATOMDB 3.0.9⁶.

⁵ The detection likelihood L is defined by $L = -\ln p$, where p is the probability that a Poissonian fluctuation of the background is detected as a spurious source.

⁶ <http://www.atomdb.org/index.php>

3.3.1 X-ray background

Detailed descriptions of the X-ray background constituents and spectral modelling can be found in, e.g. Bozzetto et al. (2014); Maggi et al. (2014); Kavanagh et al. (2015b,c, 2016); Maggi et al. (2016). As it is important for the interpretation of the plots shown in Figs. 12 and 13, we briefly describe each of the constituents here. The X-ray background consists of the astrophysical X-ray background (AXB) and particle induced background. The AXB contains contributions from the Local Hot Bubble, the Galactic halo, and unresolved active galactic nuclei (AGN). We modelled these using an unabsorbed thermal component for the Local Hot Bubble, absorbed cool and hot thermal components for the Galactic halo emission, and an absorbed power law for the unresolved background AGN (Snowden et al. 2008; Kuntz & Snowden 2010). The spectral parameters of the AGN component were fixed to the well known values of $\Gamma \sim 1.46$ and a normalisation equivalent to 10.5 photons $\text{cm}^{-2} \text{s}^{-1} \text{sr}^{-1}$ at 1 keV (Chen et al. 1997). The absorbing components comprise both Galactic and LMC contributions. The foreground Galactic absorption was fixed based on the Dickey & Lockman (1990) HI maps, determined using the HEASARC N_{H} Tool⁷. We allowed the foreground LMC absorption component, with abundances set to those of the LMC, to vary in our fits.

The particle-induced background is made up of the quiescent particle background (QPB), instrumental fluorescence lines, electronic read-out noise, and residual soft proton (SP) contamination. We constrained the contributions of the first three using FWC spectra extracted from the same detector regions as the our source and background spectra. The EPIC-pn and EPIC-MOS FWC spectra were fitted with the empirical models of Sturm (2012) and Maggi et al. (2016), respectively, using a diagonal response in XSPEC as these contributions are not subject to the instrumental response. The resulting best-fit model was included and frozen in the fits to our objects' spectra, with only the widths and normalisations of the fluorescence lines allowed to vary and a multiplicative constant to normalise the continuum of the FWC spectra. The residual SP contamination was fitted by a power law not convolved with the instrumental response as described in Kuntz & Snowden (2008).

3.3.2 Extended emission

For evolved SNRs expanding into an ISM with typical density, the spectra should contain a thermal plasma component of LMC abundance representing shock-heated ISM that has been swept-up by the blast wave. There may also be an additional component due to reverse shock-heated ejecta, which will be characterised by strong emission lines indicative of its metal content. Only the SNRs MCSNR J0504–6723 and MCSNR J0542–7104 show obviously enhanced Fe L-shell emission, consistent with the class of evolved SNRs with centrally-peaked, Fe dominated ejecta (e.g., Borkowski et al. 2006; Maggi et al. 2014; Bozzetto et al. 2014; Kavanagh et al. 2016).

We fitted the swept-up ISM contribution using both collisional ionisation equilibrium (CIE) and non-equilibrium ionisation (NEI) thermal plasma models, which were absorbed by foreground Galactic and LMC material, namely the vaped and plane-parallel vpshock models (Borkowski et al. 2001), respectively. To model pure-Fe plasma, and in some cases pure-O plasma, we used pure-metal thermal plasma models, achieved by setting all abundances

⁷ <http://heasarc.gsfc.nasa.gov/cgi-bin/Tools/w3nh/w3nh.pl>

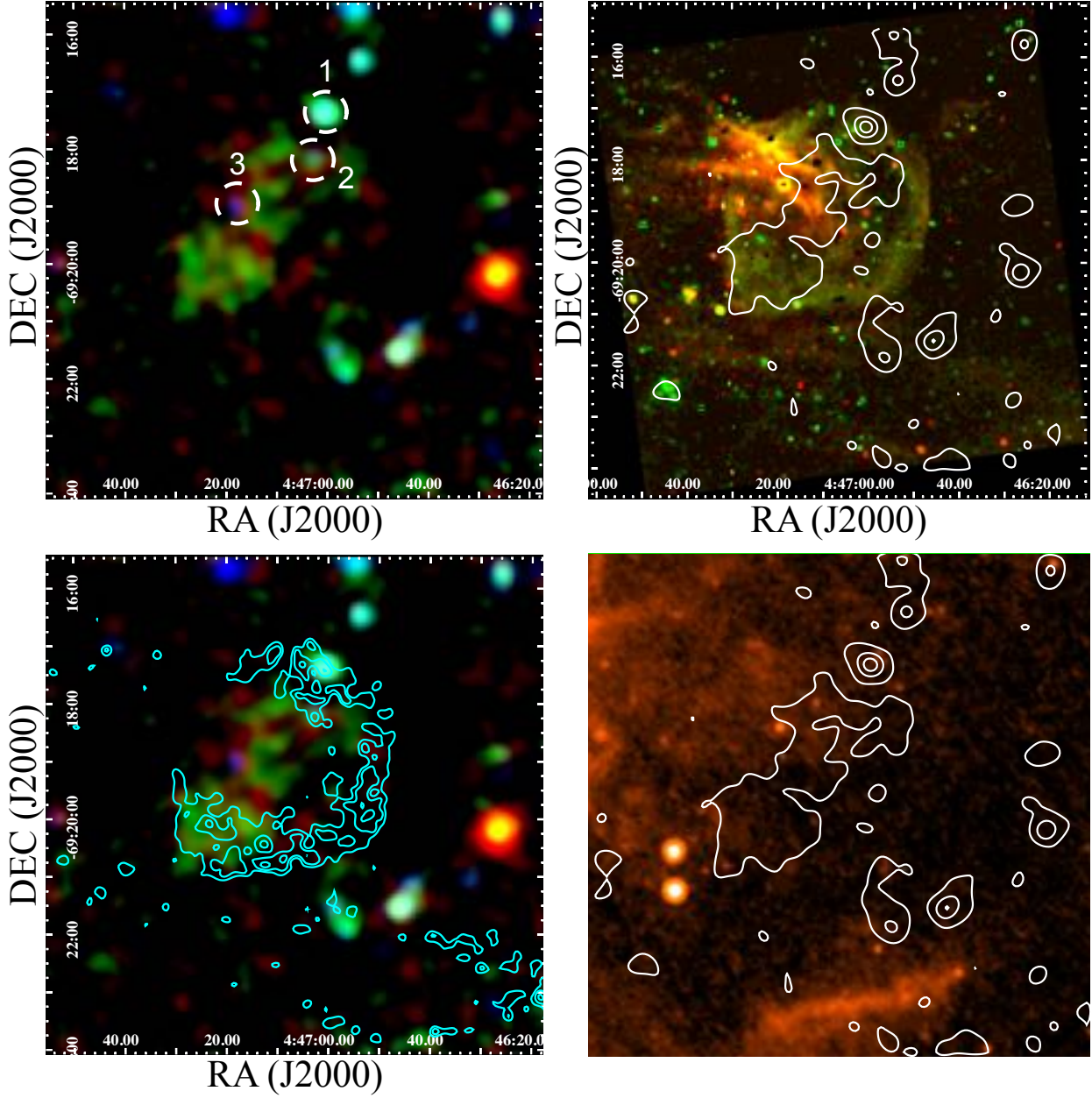


Figure 2. *Top left:* XMM-Newton EPIC image of MCSNR J0447–6919 in false colour with RGB corresponding to 0.3–0.7 keV, 0.7–1.1 keV, and 1.1–4.2 keV. Detected X-ray point sources are shown by the dashed white circles. *Top right:* Continuum-subtracted MCELS image of MCSNR J0447–6919 with $H\alpha$ in red and $[S\ II]$ shown in green overlaid with 0.3–0.7 keV contours. The lowest contour level represents 3σ above the average background surface brightness, with the remaining levels marking 25%, 50%, and 75% of the maximum above this level. *Bottom left:* Same as top left but with $[S\ II]/H\alpha$ contours with the lowest level corresponding to $[S\ II]/H\alpha = 0.4$, and the remaining levels at 25%, 50%, and 75% of the maximum above this level overlaid. *Bottom right:* Spitzer MIPS $24\ \mu\text{m}$ image of the MCSNR J0447–6919 region with the X-ray contours from top right in white. The image scale is the same as in all other panels.

apart from Fe or O to 0. A detailed description of this technique is given in Kavanagh et al. (2016). The results of our spectral fits are given in Sect. 4.

3.4 Extended source position and size

To estimate the size of the remnants we used a similar method to that described in Kavanagh et al. (2015b), which fits an ellipse to the outer X-ray contours of the SNR. While fitting the outer X-ray contours is applicable to some of our sample, it did not always repre-

sent the true extent of the object, particularly in those with no shell emission, which instead may be better traced by either the optical $[S\ II]/H\alpha$ contour (e.g. MCSNR J0447–6919), a hybrid outer contour comprising X-ray and $[S\ II]/H\alpha$ contours in different shell regions (e.g. MCSNR J0448–6700), or radio contours (e.g. MCSNR J0456–6950). More details are provided on individual cases in Sect. 4. The best-fit dimensions and errors are given in Table 6 and shown on the X-ray images in Fig. 14.

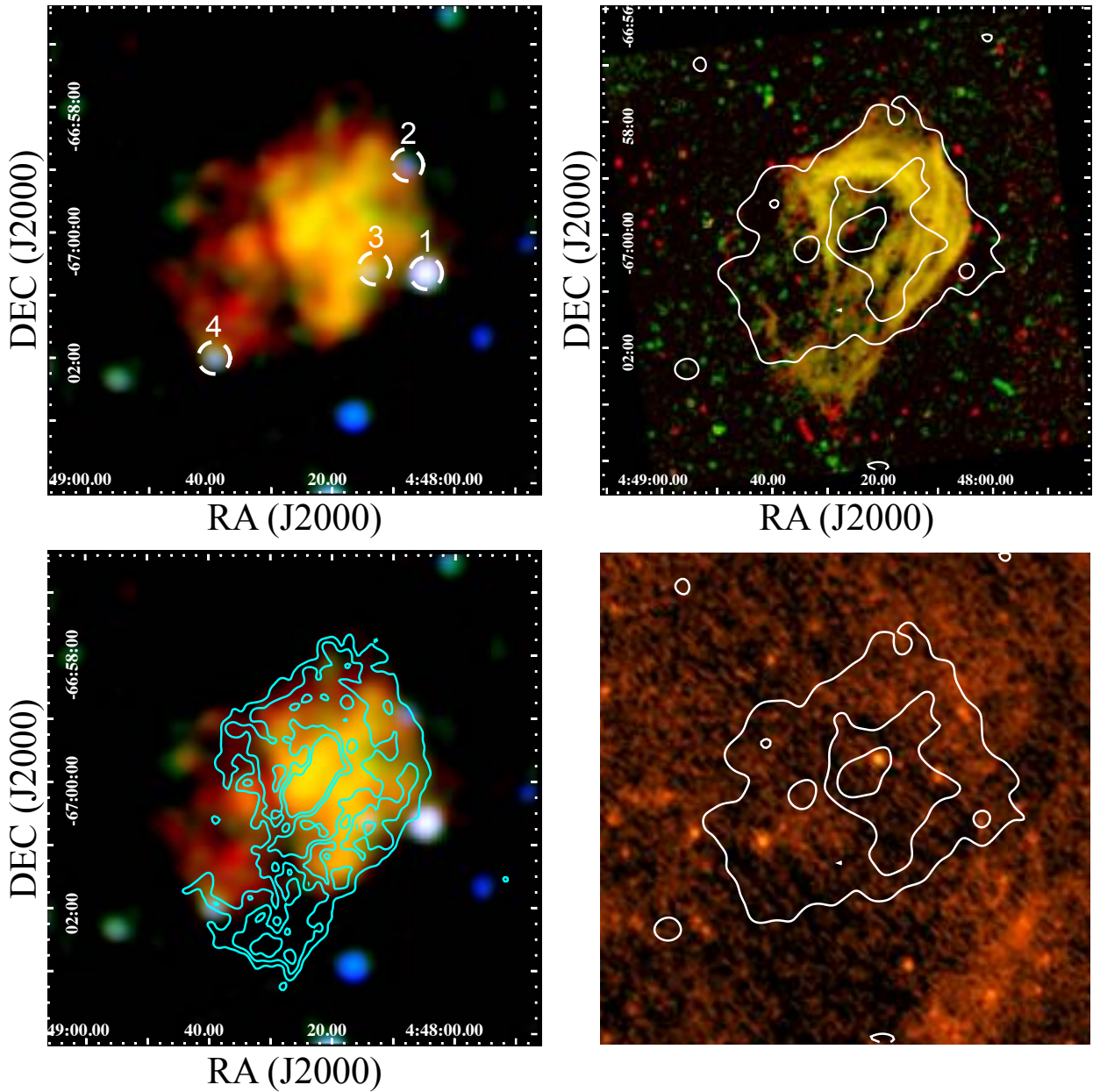


Figure 3. Same as Fig. 2 but for MCSNR J0448–6700.

3.5 MCSNR J0512–6717 optical spectroscopy

To visualise the IFU data, we extracted and collapsed sub-cubes from around the $H\alpha$ line, the $[S\text{ II}]\lambda 6716\text{\AA}, \lambda 6731\text{\AA}$ doublet, $[N\text{ II}]\lambda 6583\text{\AA}$, and $[O\text{ III}]\lambda 5007\text{\AA}$ in the full-band red or blue camera data-cubes for each field. The resulting images are shown in Fig. 15 with Field 1 shown in the top row and Field 2 in the bottom. There is clear filamentary structure evident in each field, with $H\alpha$ and $[S\text{ II}]$ images being particularly bright. We identified five regions in each field which are free from point source contamination (those sources which are evident in each emission line image of a given field) and extracted spectra from a $4'' \times 4''$ aperture centred on each position. These are shown as the boxes in Fig. 15 and sample extracted spectra are shown in Fig. 16. We then identified the $H\beta$, $H\alpha$, $[S\text{ II}]$, $[N\text{ II}]$,

and $[O\text{ III}]$ emission lines in the spectra and fitted Gaussian profiles to each.

We estimated the line fluxes for each aperture and calculated the $[N\text{ II}]/H\alpha$, $[S\text{ II}]/H\alpha$, and $[S\text{ II}]$ ratios, the values of which are indicative of the SNR nature of the filaments. The fluxes and ratios are shown for each aperture of each field in Table 7.

4 RESULTS

4.1 Non-confirmed SNRs

Only one of our SNR candidates, 0457–6739, failed to meet the criteria for SNR classification with the current data. This object was identified as a candidate SNR because faint radio continuum emis-

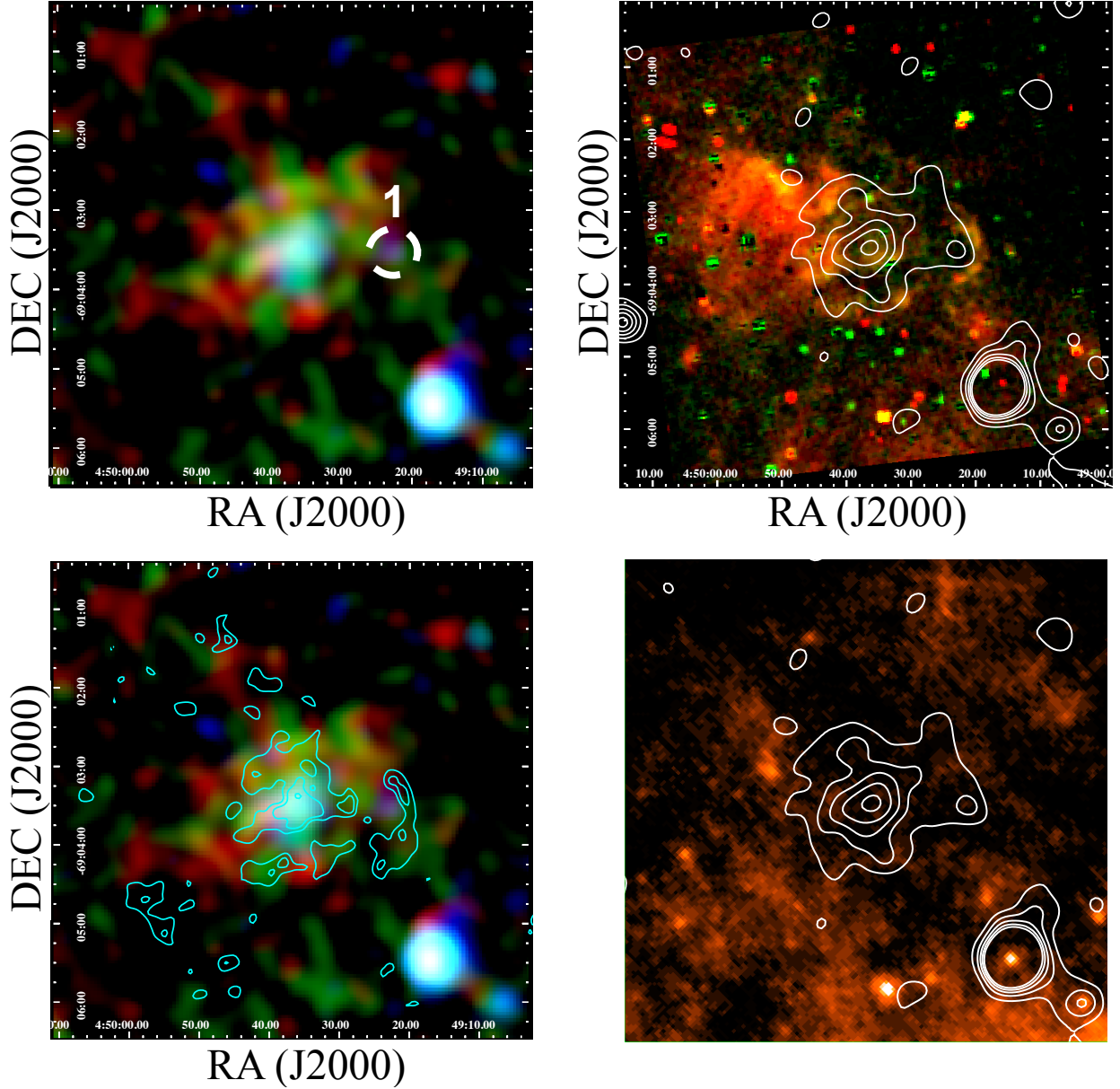


Figure 4. Same as Fig. 2 but for MCSNR J0449–6903.

sion was detected at 20 cm (Bozzetto et al. 2017). Shell-like optical emission was also detected. The multi-wavelength images of 0457–6739 are shown in Fig. 6. No X-ray emission was detected from this candidate. Bright optical emission is seen but this is inconsistent with an SNR origin with $[S\text{II}]/H\alpha < 0.4$. Sporadic regions of $[S\text{II}]/H\alpha > 0.4$ are seen which seem to trace the edge of a higher density region evident in the $24\ \mu\text{m}$ image, though appear inconsistent with an SNR shell. The faint radio emission detected from this object in Bozzetto et al. (2017) could not be determined to be non-thermal in origin. Because of the lack of a clear optical shell with enhanced $[S\text{II}]$ and X-ray emission, we cannot confirm this candidate as an SNR. We searched for this SNR candidate in our new ASKAP (Pennock et al. 2021) and ATCA (Filipović et al. 2021) high resolution and sensitivity images and we did not find any signature that may reflect the presence of SNR.

4.2 Confirmed SNRs

4.2.1 MCSNR J0447–6919

The candidate 0447–6918 was selected for our observations due to its shell-type morphology in the optical with enhanced $[S\text{II}]$ and $[S\text{II}]/H\alpha > 0.4$, indicative of an SNR. Very faint 20 cm radio continuum emission was detected in the western region, however, no reliable flux density estimate or spectral index determination was possible (Bozzetto et al. 2017, their Fig. 1, top-left). The multi-wavelength images of MCSNR J0447–6919 are shown in Fig. 2. Faint extended X-ray emission, primarily in the 0.7–1.1 keV range, is detected with a northwest-southeast elongated morphology. Bright $H\alpha$ emission is seen in the east of the remnant, along with faint, shell-like $[S\text{II}]$ emission in other regions. The $[S\text{II}]/H\alpha = 0.4$ contour shows that the eastern region bright in $H\alpha$ is not consistent with an SNR origin. However, the distinct shell seen in all other regions

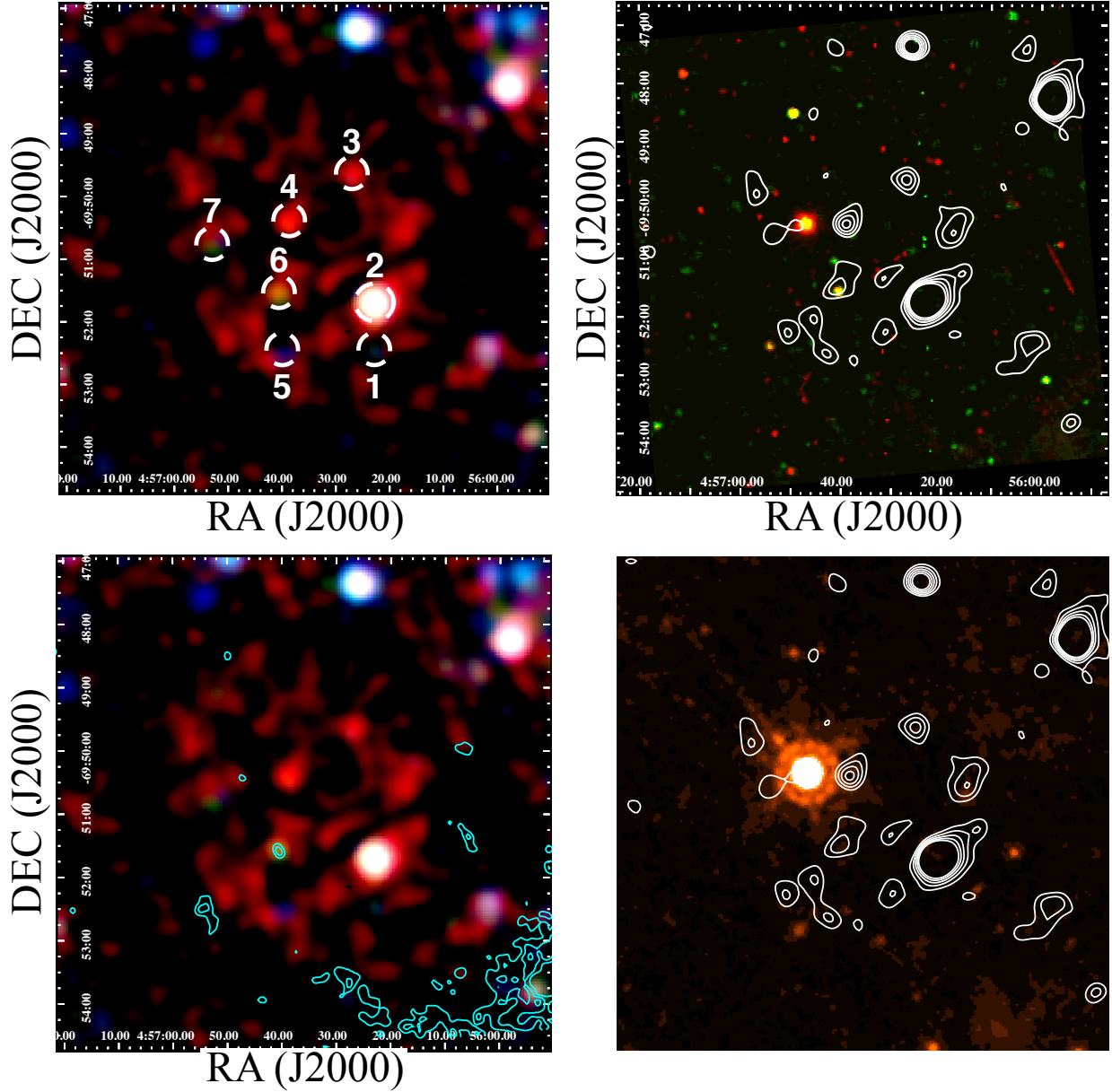


Figure 5. Same as Fig. 2 but for MCSNR J0456–6950.

shows $[\text{S II}]/\text{H}\alpha > 0.4$, indicating the presence of an SNR shock. This shell also surrounds the extended X-ray emission, appearing to confine the hot gas in the northwest and southeast regions. This observed multi-wavelength morphology is somewhat similar to MCSNR J0527–7104 (Kavanagh et al. 2016), though the X-ray emission is much fainter in MCSNR J0447–6919. There is a slight southwest-northeast ambient density gradient evident from the $24\ \mu\text{m}$ image. This may explain the slight ovality and brightness variation in the optical morphology, with the shell appearing fainter and more extended into the lower density region. We estimated the SNR position and size using the outer $[\text{S II}]/\text{H}\alpha > 0.4$ contour, omitting the region bright in $\text{H}\alpha$ to the east, the results of which are given in Table 6. The size was found to be 54.58×59.76 (± 2.37) pc, which is consistent with evolved SNRs in the LMC.

Given the emission from MCSNR J0447–6919 is quite faint, we initially fitted the X-ray spectrum with an NEI thermal plasma model

(*vpshock* in XSPEC) of LMC abundance. While this provided a good fit to the data ($\chi^2_\nu = 1.10$, see Table 3), there were obvious residuals $\gtrsim 0.8$ keV where the Fe L-shell complex might dominate. We therefore performed trial fits with the Fe abundances allowed to vary to determine if it is enhanced compared to the LMC value. This provided a slightly better fit to the data ($\chi^2_\nu = 1.03$) and suggests an overabundance of Fe (see Table 3 and Fig. 12). However, the X-ray emission in MCSNR J0447–6919 is too faint to perform a more detailed multi-component spectral analysis. The best fit plasma temperatures in both fits are low $kT < 0.3$ keV which is consistent with an evolved remnant. For the model with LMC abundance, $\tau \sim 10^{11}$ s cm^{-3} which suggests the plasma is close to, but yet to reach CIE. However, this value could misrepresent the true state of the plasma given the better fit with variable Fe abundance. The value of τ in this variable Fe fit ($\tau \gtrsim 10^{11}$ s cm^{-3}) indicates a plasma close to or in CIE. Unfortunately, the poor statistics do not allow for better

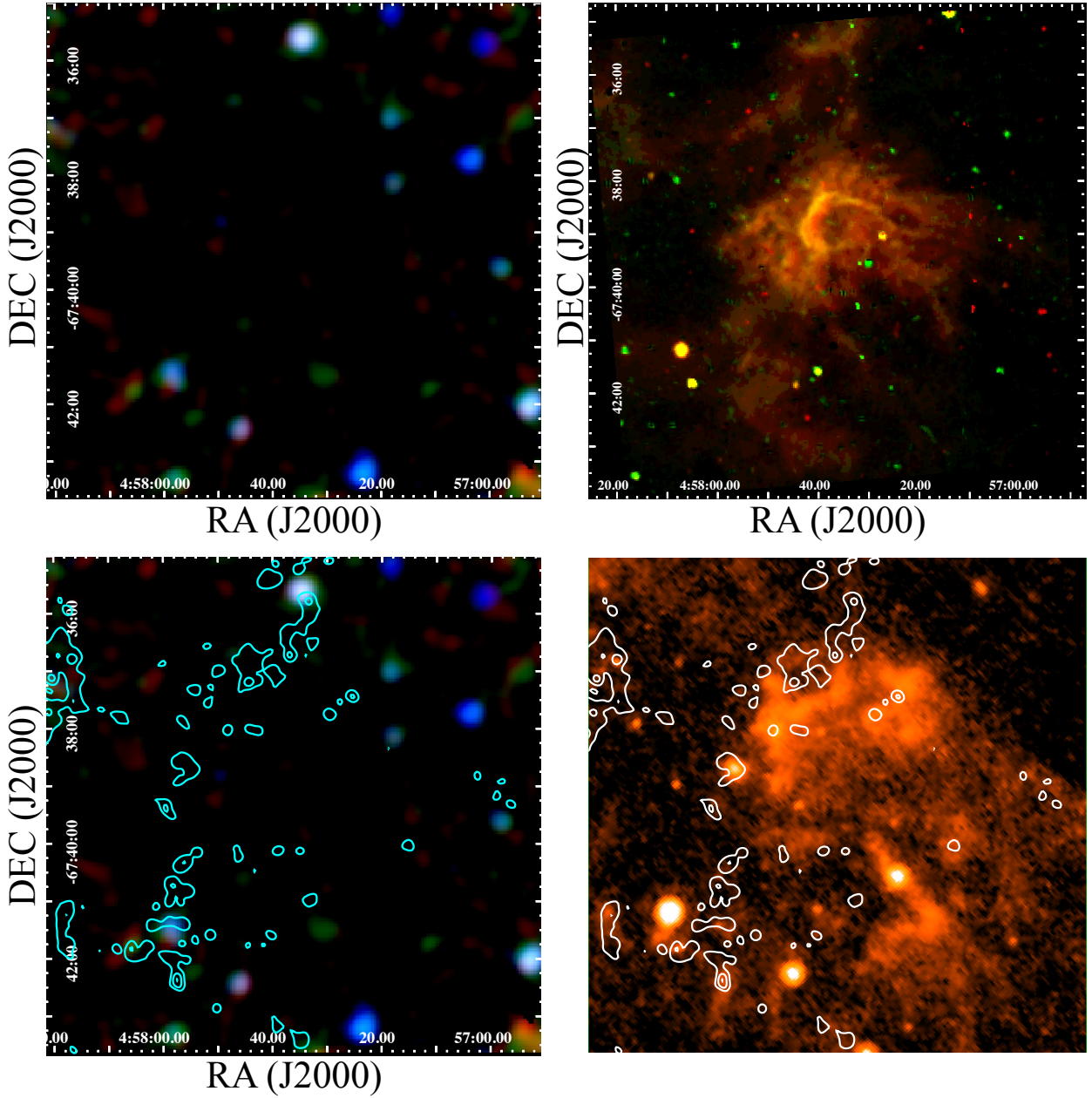


Figure 6. Same as Fig. 2 but for 0457–6739.

constraints on τ and a more definitive conclusion. The detection of extended, thermal X-ray emission and the shell with $[\text{S II}]/\text{H}\alpha > 0.4$ confirms this object as an SNR.

4.2.2 MCSNR J0448–6700

The object [HP99] 460 was detected by *ROSAT* and classified as an SNR candidate based on its extent of $46.3''$ (Haberl & Pietsch 1999). It was firmly detected in radio as an extended and circular object of diameter $\sim 4'$, though with a somewhat flat spectral index $\alpha = -0.11 \pm 0.05$. Because of the radio and X-ray detections, this object was classified as an SNR in both Maggi et al. (2016) and Bozzetto et al. (2017), now carrying the identifier MCSNR J0448–6700. The multi-wavelength images of this object are shown in Fig. 3. Ex-

tended X-ray emission is clearly observed with the emission being brighter towards the west. A similar brightening is seen in the optical emission line images, though the morphology is more shell-like than the X-ray. The $[\text{S II}]/\text{H}\alpha = 0.4$ contour shows the characteristic SNR value towards the west and south. There is no appreciable variation in the ambient density from the $24 \mu\text{m}$ image though the optical and X-ray morphologies do suggest some ambient density variation. Such a variation could have been induced if the SN progenitor was a runaway massive star with a proper motion in an approximate east-to-west direction, with the bow-shock of the SN progenitor wind providing the higher density in the west (Meyer et al. 2015). We used a hybrid contour combining the outer 0.3–0.7 keV and $[\text{S II}]/\text{H}\alpha = 0.4$ contours to determine the position and size of the remnant, with the results shown in Table 6. The size was found to be

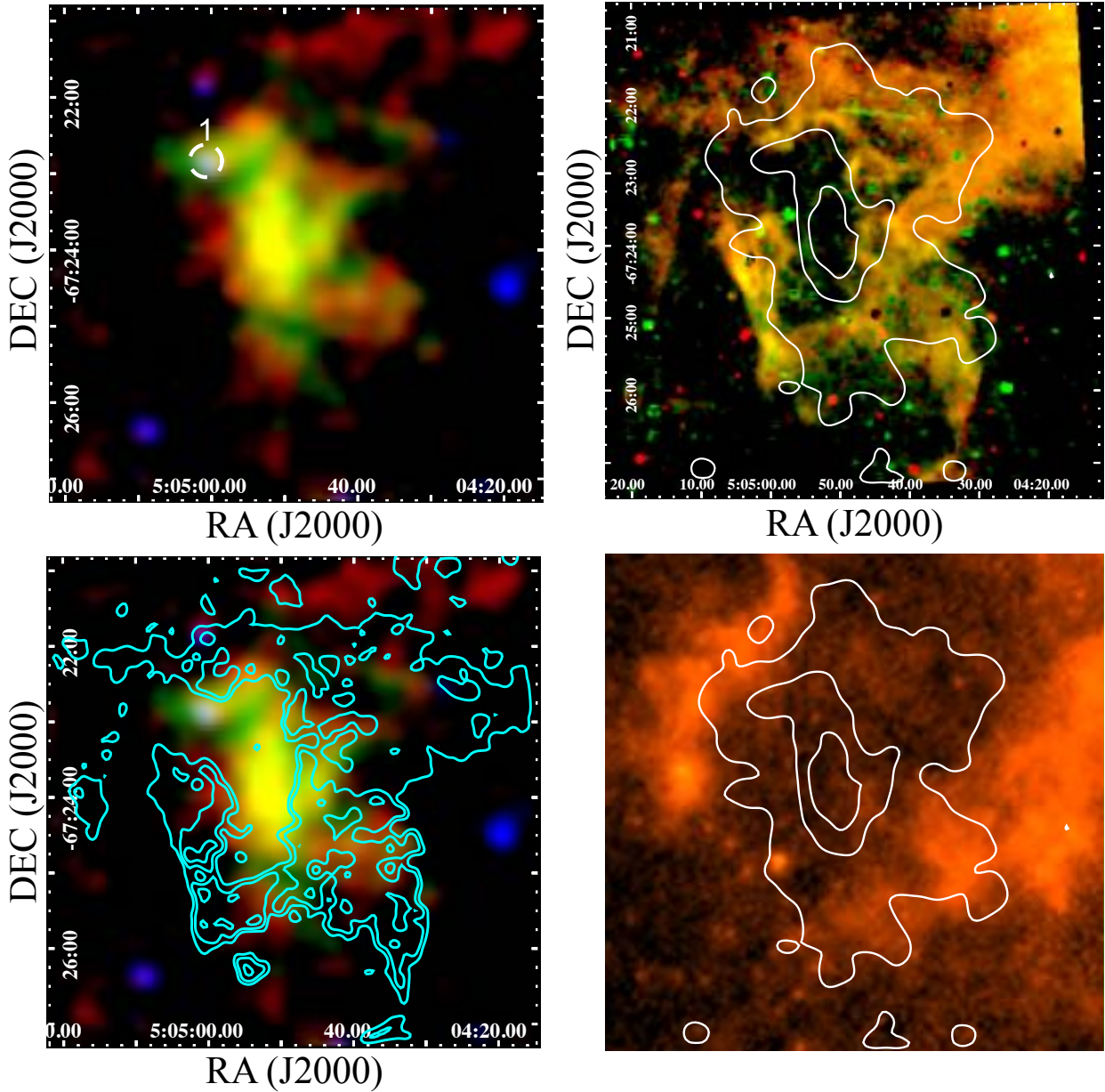


Figure 7. Same as Fig. 2 but for MCSNR J0504–6723.

$55.54 \times 77.32 (\pm 7.15)$ pc, which is consistent with evolved SNRs in the LMC.

We fitted the X-ray emission from MCSNR J0448–6700 using the *vpshock* model allowing the abundances of O, Ne, Mg, and Fe to vary, and all others fixed to the LMC abundance. Trial fits with other elemental abundances free did not allow for constraints on the parameters. This yielded an acceptable fit with $\chi^2_\nu = 1.28$ (see Table 3 and Fig. 12). The best fit $kT \sim 0.2$ keV and $\tau \gtrsim 10^{12}$ s cm^{-3} are consistent with an evolved SNR with CIE well established. The fitted abundances are consistent with those in the swept-up ISM in other LMC SNRs (e.g. Maggi et al. 2016, their Table 5).

4.2.3 MCSNR J0449–6903

The candidate 0449–6903 was detected in 36 cm, 20 cm, and 6 cm radio continuum, with a spectral index $\alpha = -0.50 \pm 0.01$, typical of evolved SNRs (Bozzetto et al. 2017, their Fig. 1, top-left). Optical emission was also detected at the northeastern edge of the radio emission. The multi-wavelength images of this object are shown in Fig. 4. Extended X-ray emission is detected with a centrally filled morphology. Interestingly, hard X-ray emission (> 1.1 keV) is detected from the core region. Sporadic optical emission with $[\text{S II}]/\text{H}\alpha > 0.4$ was detected though did not trace a typical SNR shell morphology, though there is some evidence of a shell to the south and southeast which encloses the X-ray emission. There is no indication of ambient density variation from the $24 \mu\text{m}$ image. We used the outer 0.3–1.1 keV contour to determine the position and size of the remnant, given in Table 6. The size was found to be

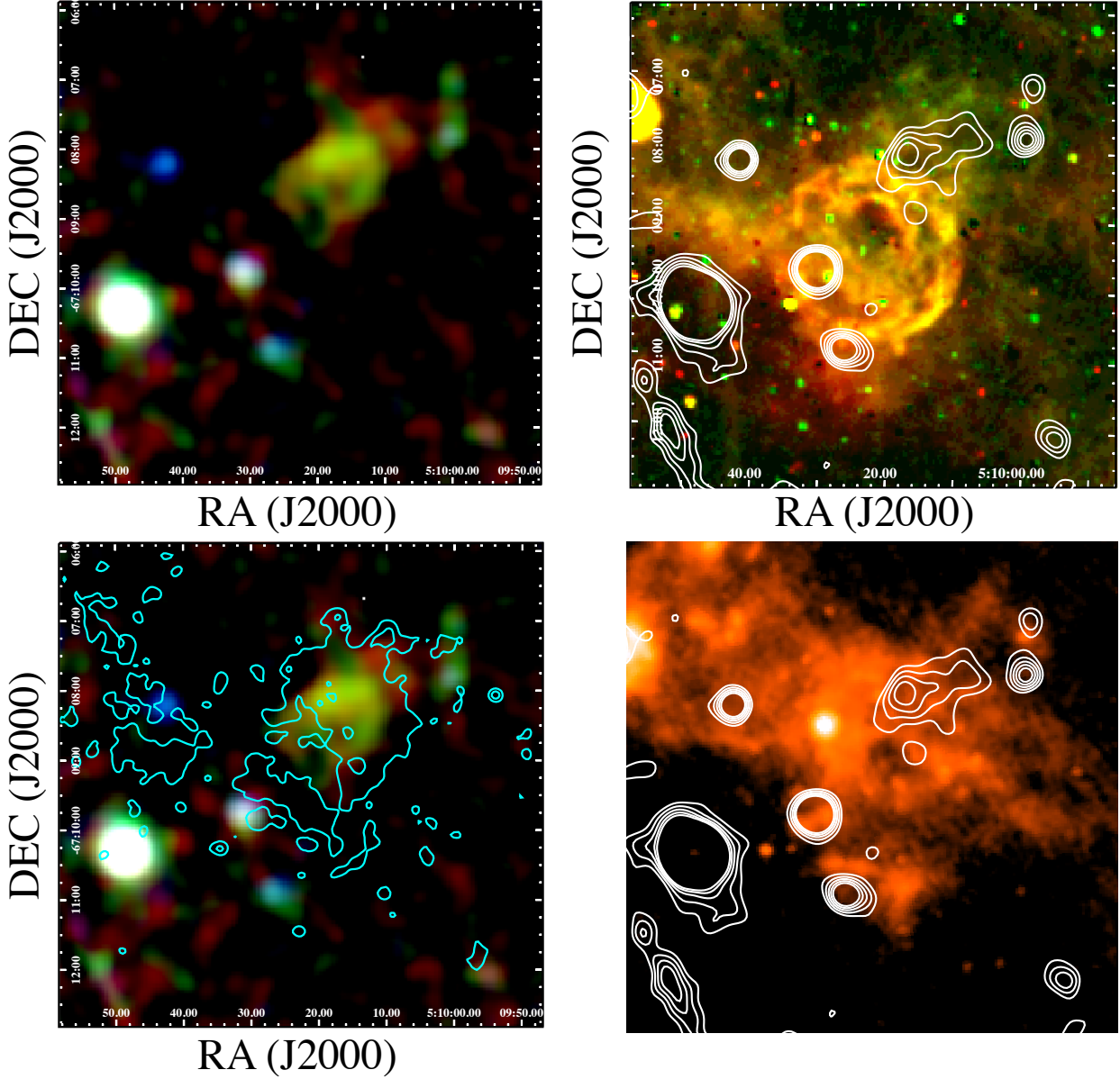


Figure 8. Same as Fig. 2 but for MCSNR J0510–6708.

$33.97 \times 26.34 (\pm 3.37)$ pc, the smallest SNR in our sample but also one of the faintest.

We performed trial fits of the spectra using single component thermal plasma models of LMC abundance in both CIE and NEI. The CIE fit was poor with significant residuals in the 0.5–0.7 keV range. While the NEI fit was statistically better, the best fit plasma temperature was much higher than expected from a faint, evolved SNR ($kT > 4$ keV). Further fits with selected α -group and Fe free showed some minor improvements but the abundance parameters could not be constrained to any reasonable degree. Given that the morphology suggests two distinct emission structures, i.e. the shell and the core, we tried fitting two thermal plasma components. Trial fits with two NEI plasmas with the ionisation parameters of one or both components free did not provide constraints on many of the fit parameters. For this reason, we fitted a two component CIE model to the spectra. This provided a good fit to the data ($\chi^2_{\nu} = 1.10$), the results of

which are presented in Table 5 and shown in Fig. 13 left. The low temperature component with $kT=0.26$ (0.21–0.37) keV is consistent with an evolved SNR shell. The higher temperature component with $kT=2.81$ (2.06–4.60) keV suggests hotter ejecta emission but there is no evidence for enhanced abundances which should be present if the emission is due to hot ejecta. We also tried a thermal plasma (CIE) plus non-thermal (power law) model to fit the spectrum of the SNR. This also provided a good fit to the data ($\chi^2_{\nu} = 1.09$), the results of which are given in Table 5 and shown in Fig. 13 right. Again, the temperature of the soft thermal model suggests an evolved SNR shell ($kT=0.17$ (0.05–0.26) keV). It is unclear as to what could be the origin of non-thermal emission in the SNR.

We investigated the extent of the hard X-ray emission by extracting a radial profile from the 1.1–4.2 keV image, centred on the brightest region of the hard emission, in $10''$ bins. To show that the source is indeed extended, we generated an EPIC-pn PSF using

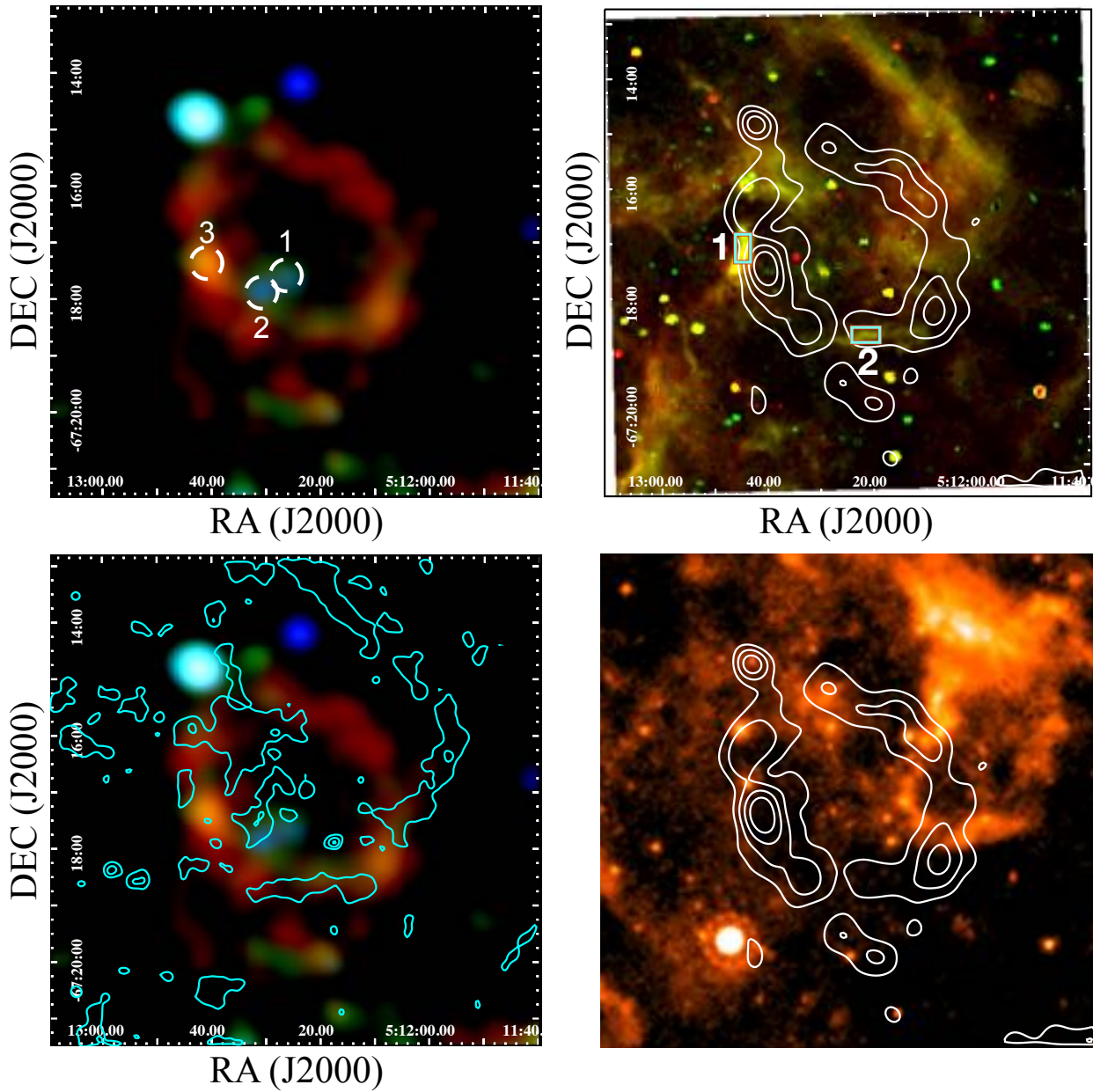


Figure 9. Same as Fig. 2 but for MCSNR J0512–6717. The numbered cyan boxes in top-right indicate the WiFeS fields from which spectroscopic data were obtained.

the SAS task `psfgen` at 2.5 keV and applied the same convolution as used for the 1.1–4.2 keV image. Both the radial profile and the PSF are shown in Fig. 17. The hard source is clearly larger than the PSF, with a profile radius of $1.16 (\pm 0.08)'$, which corresponds to $\sim 16.9 (\pm 1.1)$ pc at the LMC distance. This size is comparable to the dimensions of the SNR (Table 6) so the hard emission appears to fill the SNR shell. The nature of this source is discussed in more detail in Sect. 5.4.2.

Given the X-ray and optical detection in this work, and the radio detection reported in Bozzetto et al. (2017), we confirmed the SNR nature of this object.

4.2.4 MCSNR J0456–6950

The candidate 0456–6951 was identified as a potential radio SNR based on a shell-like radio structure (Bozzetto et al. 2017). No clear optical counterpart to the shell could be found though there is extended optical emission around the candidate. The multi-wavelength images of MCSNR J0456–6950 are shown in Fig. 5. A very faint extended source is evident in the 0.3–0.7 keV X-ray band. However, the emission is so faint it largely falls below the 3σ threshold used in Sect. 3.4 to estimate the SNR dimensions. Similarly, no optical shell or filaments are evident from the MCELS images. The $[\text{S II}]/\text{H}\alpha$ contour does reveal some patchy regions with $[\text{S II}]/\text{H}\alpha > 0.4$ to the south and southwest which appear to delineate the edge of the faint extended X-ray emission and suggests an association. We searched for radio emission from this object in our new ASKAP images (Pen-

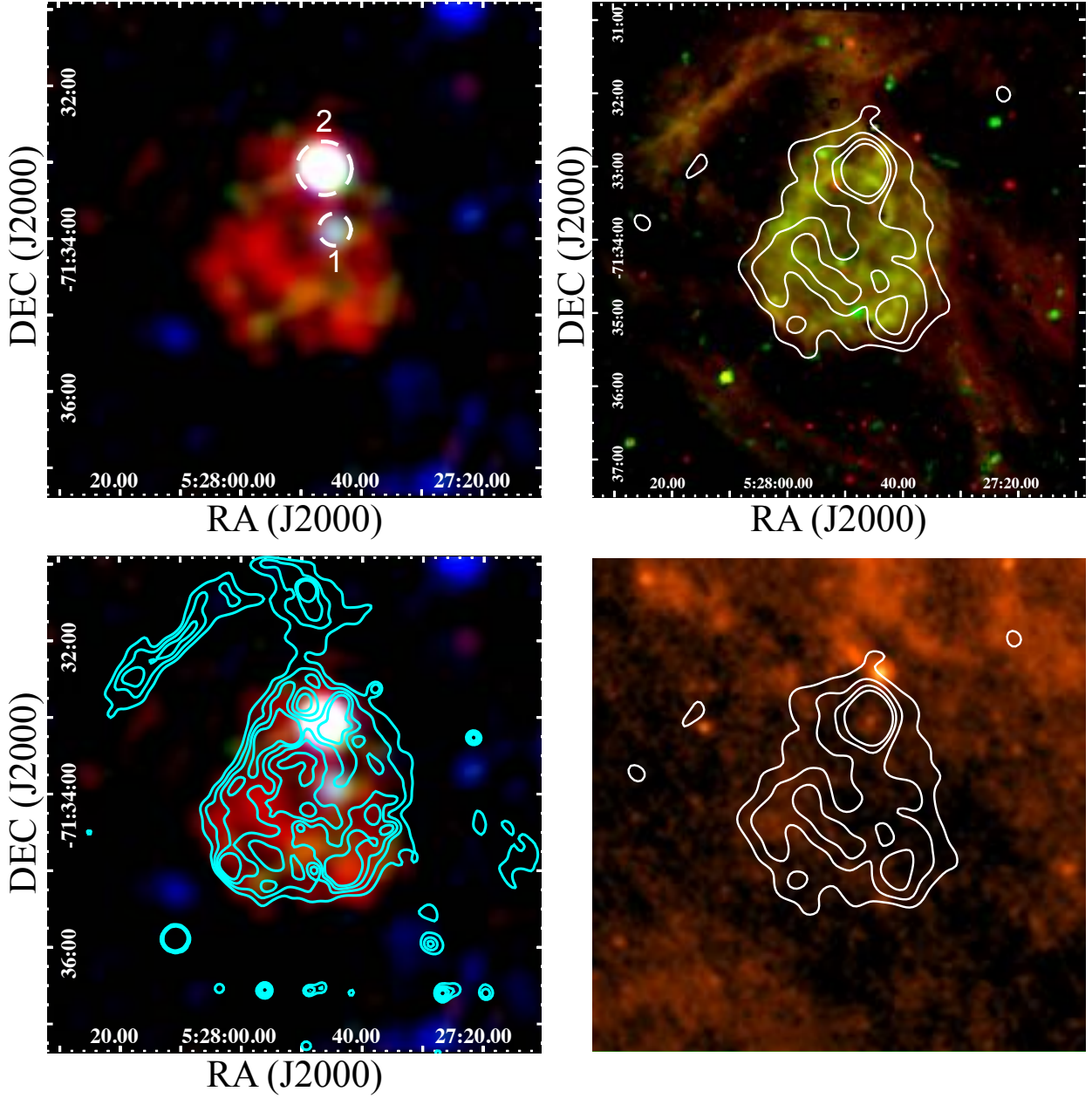


Figure 10. Same as Fig. 2 but for MCSNR J0527–7134.

nock et al. 2021) which revealed a circular radio shell coincident with the X-ray emission, shown in Fig. 18. This radio emission offers a much improved view of the size and shape of this SNR. We therefore determine its position and size using the radio contour, given in Table 6 with the fit shown in Fig. 14. The size was found to be $65.80 \times 62.26 (\pm 1.80)$ pc, which is consistent with an evolved LMC SNR.

We initially fitted the X-ray emission from MCSNR J0456–6950 using the *vpshock* model, however we could not constrain the ionisation timescale. Given the large size of the remnant, it is likely a very evolved SNR and we assumed that the plasma has reached CIE and fixed the ionisation timescale in our fits to 10^{12} cm s⁻³. This model provided an acceptable fit ($\chi^2_\nu = 1.15$, see Table 3). The best fit temperature of 0.14 (0.13–0.16) keV is consistent with an evolved

SNR. With the detection of extended thermal X-ray emission, sparse regions with $[\text{S II}]/\text{H}\alpha > 0.4$, and the clear ASKAP detection, we confirmed this object as an SNR.

4.2.5 MCSNR J0504–6723

The object [HP99] 529 was detected by *ROSAT* and classified as an SNR candidate based on its extent and hardness ratios (Haberl & Pietsch 1999). No radio emission from this object was detected in the study of Bozzetto et al. (2017). The multi-wavelength images of this object are shown in Fig. 7. Significant extended X-ray emission is detected with a centrally-filled morphology. The emission is elongated in a southwest-northeast direction. Interestingly, the 0.7–1.1 keV emission is mostly detected at the centre while the softer

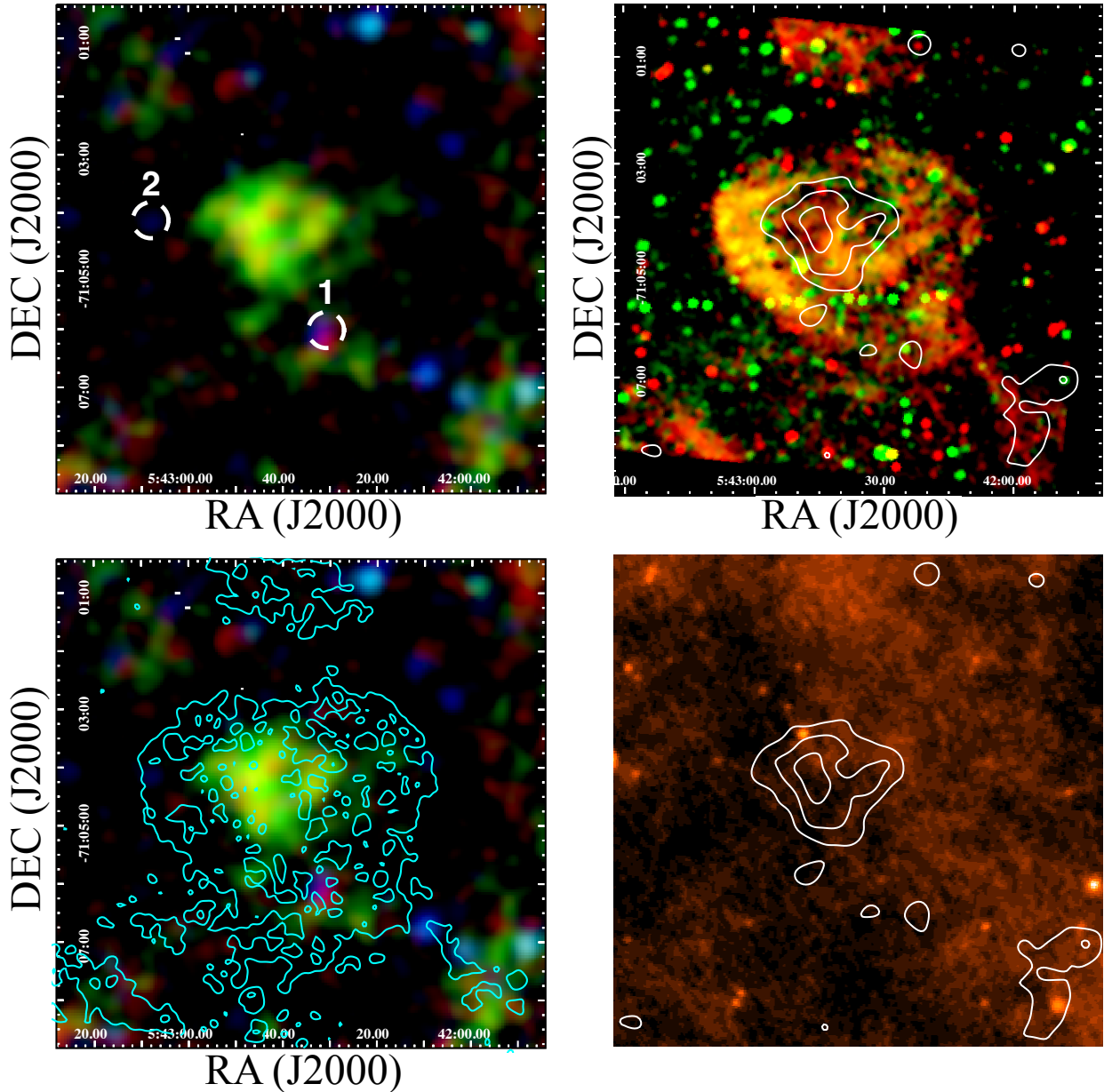


Figure 11. Same as Fig. 2 but for MCSNR J0542–7104.

0.3–0.7 keV emission is detected in the outer regions. This suggests that MCSNR J0504–6723 might belong to the class of evolved SNRs with enhanced Fe emission (e.g., [Bozzetto et al. 2014](#); [Maggi et al. 2014](#); [Kavanagh et al. 2016](#)). However, the morphology of MCSNR J0504–6723 appears far more dispersed than other remnants in the class with the Fe-rich material less confined to the core region. Significant optical emission is detected around the X-ray emission with $[\text{S II}]/\text{H}\alpha > 0.4$, indicative of an SNR origin. The optical emission has an unusual morphology, appearing more rectangular than circular. The $24 \mu\text{m}$ image reveals the likely reason for this with higher density regions appearing to confine the SNR in the northeast and southwest quadrants. The optical and X-ray morphology suggests the southeast emission is also confined while the remnant is free to expand in the northwest through a low density channel, similar to the asymmetric expansion proposed for MCSNR J0517–

6759 ([Maggi et al. 2014](#)). We used a hybrid contour combining the outer 0.3–1.1 keV and $[\text{S II}]/\text{H}\alpha = 0.4$ contours to determine the position and size of the remnant, with the results shown in Table 6 and shown in Fig. 14. The size was found to be $58.00 \times 75.62 (\pm 7.71)$ pc, which is consistent with evolved SNRs in the LMC.

To demonstrate the overabundance of Fe we initially fitted the X-ray spectrum with the vpshock model, which resulted in a poor fit ($\chi^2_{\nu} = 1.56$) with significant residuals between ~ 0.8 – 0.9 keV. We then allowed the Fe abundance to vary, resulting in an acceptable fit ($\chi^2_{\nu} = 1.29$) with an Fe abundance of $(Z/Z_{\odot})_{\text{Fe}} = 2.44$ (1.90–4.32) and a high $kT = 0.72$ (0.68–0.99) keV. We also tried freeing Ne on its own and in combination with Fe as it can be hard to distinguish between enhanced Ne and Fe in the 0.8–0.9 keV range. The fit with Ne free resulted in a very poor fit. Freeing both Ne and Fe resulted in as statistically good a fit as with only Fe free ($\chi^2_{\nu} = 1.20$) though

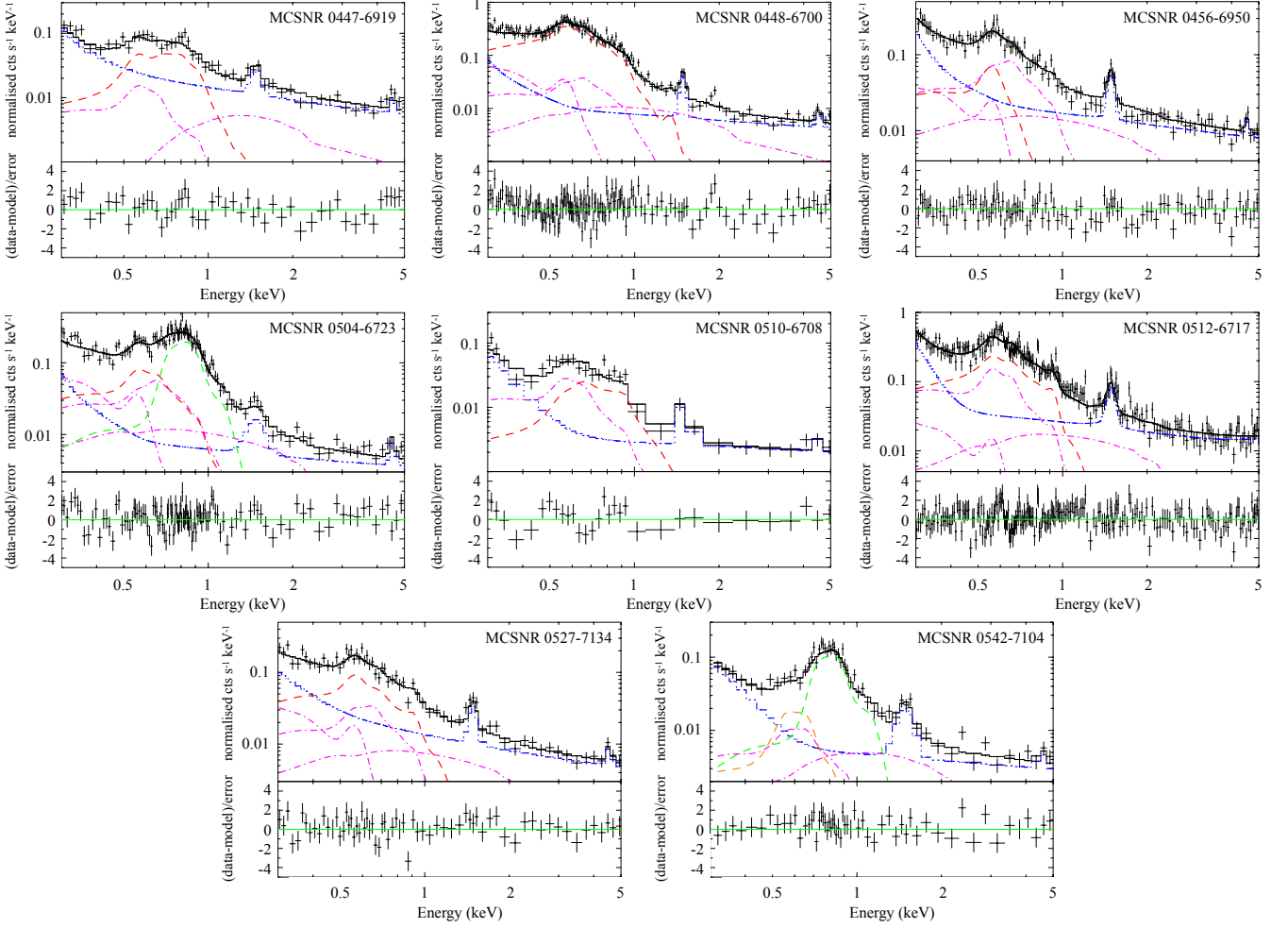


Figure 12. X-ray spectral fits to our SNR sample. The dashed red line shows the fitted thermal plasma component, the magenta dash-dot lines indicate the AXB components, and the blue dash-dot-dot-dot line shows the combined contributions of the QPB, instrumental fluorescence lines, and electronic noise. In the cases of MCSNR J0504–6723 and MCSNR J0542–7104, the green and orange dashed lines represent the pure Fe and pure O components, respectively.

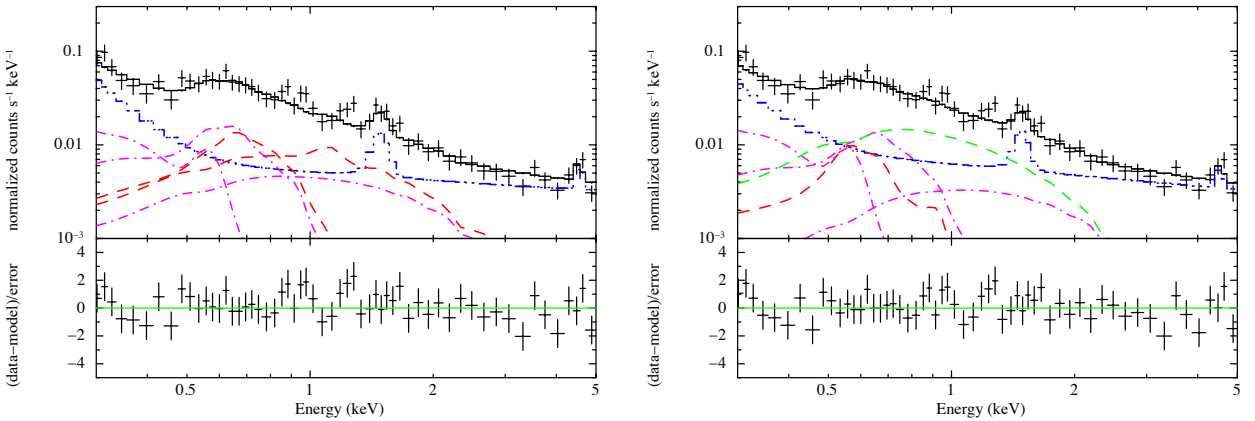


Figure 13. Two-component X-ray spectral fits to the spectrum of MCSNR J0449–6903. *Left:* The absorbed two-temperature thermal plasma model ($\text{vphabs}^*(\text{vapec}+\text{vapec})$). The dashed red lines show the fitted thermal plasma components, the magenta dash-dot lines indicate the AXB components, and the blue dash-dot-dot-dot line shows the combined contributions of the QPB, instrumental fluorescence lines, and electronic noise. *Right:* The absorbed thermal plus non-thermal component fit ($\text{vphabs}^*(\text{vapec}+\text{pow})$). The lines have the same meaning as in *Left* except the green dashed line represents the non-thermal component.

Table 3. Single component X-ray spectral fit results to our SNR sample. Fits with CIE under the τ column are `vphabs*vapec` models while fits with a numeric τ value are `vphabs*vpshock` models.

$N_{\text{H}}^{(a)}$ (10^{22} cm^{-2})	kT (keV)	τ ($10^{11} \text{ s cm}^{-3}$)	Abundances (Z/Z_{\odot})	χ^2_{ν} (d.o.f.)	EM (10^{57} cm^{-3})	$\log F_{\text{X}}^{(b)}$ ($\text{erg cm}^{-2} \text{ s}^{-1}$)	$\log L_{\text{X}}^{(c)}$ (erg s^{-1})
MCSNR J0447–6919							
0.59 (0.46–0.73)	0.23 (0.20–0.30)	2.63 (0.90–8.62)	W00	1.10 (290)	10.11 (4.17–21.43)	-13.57	35.16
0.70 (0.58–0.82)	0.15 (0.14–0.19)	5.26 (> 0.86)	Fe: 14.15 (> 1.40)	1.03 (289)	43.92 (18.14–122.26)	-13.38	35.49
MCSNR J0448–6700							
0.14 (0.09–0.19)	0.19 (0.18–0.21)	> 17.85	O: 0.25 (0.20–0.33) Ne: 0.32 (0.21–0.47) Mg: 0.83 (0.21–1.74) Fe: 0.61 (0.35–0.84)	1.28 (357)	32.71 (21.22–48.71)	-12.81	35.18
MCSNR J0456–6950							
< 0.04	0.14 (0.12–0.16)	CIE	W00	1.15 (479)	3.05 (2.24–5.17)	-13.65	34.11
MCSNR J0510–6708							
0.73 (0.28–0.99)	0.20 (0.16–0.32)	CIE	W00	1.01 (70)	9.83 (1.11–47.62)	-13.87	34.92
MCSNR J0512–6717							
0.14 (0.09–0.21)	0.19 (0.18–0.21)	CIE	O: 0.25 (0.19–0.31) Fe: 0.60 (0.33–1.10)	1.14 (914)	20.04 (13.80–32.93)	-12.97	35.02
MCSNR J0527–7134							
0.02 (< 0.14)	0.53 (0.19–1.32)	0.26 (0.09–12.66)	O: 0.36 (0.19–0.59) Ne: 0.53 (0.21–1.00)	0.97 (271)	0.71 (0.36–3.53)	-13.37	34.43
0.06 (< 0.17)	0.19 (0.18–0.21)	CIE	O: 0.22 (0.12–0.41) Ne: 0.59 (0.28–1.19)	0.98 (272)	7.19 (3.28–17.92)	-13.38	34.54

Notes: The numbers in parentheses are the 90% confidence intervals. ^(a) Absorption abundances fixed to those of the LMC. ^(b) 0.3–8 keV absorbed X-ray flux. ^(c) 0.3–8 keV de-absorbed X-ray luminosity, adopting a distance of 50 kpc to the LMC. W00 refers to [Wilms et al. \(2000\)](#), see text).**Table 4.** X-ray spectral fit results for the Fe-rich SNRs.

$N_{\text{H}}^{(a)}$ (10^{22} cm^{-2})	kT_{sh} (keV)	EM_{sh} (10^{57} cm^{-3})	kT_{Fe} (keV)	EM_{Fe} (10^{52} cm^{-3})	kT_{O} (keV)	EM_{O} (10^{53} cm^{-3})	χ^2_{ν} (d.o.f.)	$\log F_{\text{X}}^{(b)}$ ($\text{erg cm}^{-2} \text{ s}^{-1}$)	$\log L_{\text{X}}^{(c)}$ (erg s^{-1})
MCSNR J0504–6723									
Model: <code>vphabs*(vpshock+vnei_{Fe})</code>									
0.04 (< 0.11)	0.24 (0.20–0.34)	1.80 (1.30–2.78)	0.68 (0.66–0.71)	9.23 (7.35–10.71)	–	–	1.20 (324)	-13.00	34.63
Model: <code>vphabs*(vpshock+vnei_{Fe}+vnei_O)</code>									
0.04 (< 0.10)	0.24 (0.18–0.34)	1.78 (1.25–2.78)	0.68 (0.66–0.71)	9.22 (7.56–10.73)	= kT_{Fe}	0.03 (<19.53)	1.20 (323)	-13.00	34.63
MCSNR J0542–7104									
Model: <code>vphabs*(vnei_{Fe})</code>									
0.16 (0.08–0.26)	–	–	–	0.57 (0.55–0.60)	7.55 (6.27–9.39)	–	1.25 (402)	-13.42	34.28
Model: <code>vphabs*(vnei_{Fe}+vnei_O)</code>									
0.26 (0.16–0.37)	–	–	0.58 (0.54–0.62)	8.58 (6.89–10.91)	0.19 (0.14–0.24)	9.06 (4.33–21.03)	1.02 (402)	-13.38	34.46

Notes: The numbers in parentheses are the 90% confidence intervals. ^(a) Absorption abundances fixed to those of the LMC. ^(b) 0.3–8 keV absorbed X-ray flux. ^(c) 0.3–8 keV de-absorbed X-ray luminosity, adopting a distance of 50 kpc to the LMC. The ionisation parameter for the `vpshock` component in the fits (τ_{sh}) was fixed to $10^{12} \text{ s cm}^{-3}$ representing a plasma in CIE (see text).

the abundance of Fe was clearly enhanced $(Z/Z_{\odot})_{\text{Fe}} \gtrsim 1.9$ while the Ne abundance was consistent with the LMC value. For this reason, we proceed under the assumption that the emission is Fe dominated.

We then took the same approach as for other similar objects of fitting the ejecta emission with spectral components comprising pure Fe, and possibly O (e.g. [Maggi et al. 2014, 2016](#); [Kavanagh et al. 2016](#)), represented by the `vnei` model with Fe abundance set to

1000 and all others to 0 (see [Kavanagh et al. 2016](#), for a description of the model employed). The shell emission was modelled using a `vpshock` model of LMC abundance. We initially tried allowing the ionisation timescales of both the shell and ejecta components and the shell abundances to vary, however we could not constrain any of these parameters. We therefore assumed that both the shell and ejecta components were in CIE, fixing $\tau = 10^{12} \text{ cm s}^{-3}$, and set the

Table 5. MCSNR J0449–6903 two-component X-ray spectral fit results.

$N_{\text{H}}^{(a)}$ (10^{22} cm $^{-2}$)	kT_1 (keV)	EM_1 (10^{57} cm $^{-3}$)	kT_2 (keV)	Γ	EM_2 (10^{57} cm $^{-3}$)	$norm.$ (10^{-5} cm $^{-5}$)	χ^2_{ν} (d.o.f.)	$\log F_X^{(b)}$ (erg cm $^{-2}$ s $^{-1}$)	$\log L_X^{(c)}$ (erg s $^{-1}$)
Model: vphabs*(vapec+vapec)									
0.11 (0.04–0.22)	0.26 (0.21–0.37)	0.55 (0.25–1.21)	2.81 (2.06–4.60)	–	0.91 (0.74–1.07)	–	1.10 (224)	-13.44	34.20
Model: vphabs*(vapec+powerlaw)									
0.27 (0.15–0.44)	0.17 (0.05–0.26)	1.11 (0.06–7.99)	–	2.82 (2.34–3.35)	–	1.54 (1.16–2.03)	1.09 (224)	-13.46	34.46

Notes: The numbers in parentheses are the 90% confidence intervals. ^(a) Absorption abundances fixed to those of the LMC. ^(b) 0.3–8 keV absorbed X-ray flux. ^(c) 0.3–8 keV de-absorbed X-ray luminosity, adopting a distance of 50 kpc to the LMC.

Table 6. Best fit position and dimensions of the SNR sample.

ID	RA (J2000)	Dec (J2000)	$D_{\text{maj}} \times D_{\text{min}}$ (arcsec)	$D_{\text{maj}} \times D_{\text{min}}$ (pc)	PA (degrees EoN)
MCSNR J0447–6919	04:47:10.26	-69:19:07.4	246.6×225.0 (± 9.6)	59.76×54.58 (± 2.37)	147.6
MCSNR J0448–6700	04:48:25.65	-67:00:22.1	319.2×229.2 (± 29.4)	77.32×55.54 (± 7.15)	146.0
MCSNR J0449–6903	04:49:35.47	-69:03:25.6	140.4×108.6 (± 13.8)	33.97×26.34 (± 3.37)	108.1
MCSNR J0456–6950	04:56:38.55	-69:50:44.1	271.5×256.8 (± 7.6)	65.80×62.26 (± 1.80)	151.5
MCSNR J0504–6723	05:04:49.18	-67:23:51.0	312.0×239.4 (± 31.8)	75.62×58.00 (± 7.71)	21.2
MCSNR J0510–6708	05:10:18.59	-67:08:38.0	193.8×121.2 (± 24.6)	47.03×29.46 (± 5.92)	155.9
MCSNR J0512–6717	05:12:24.35	-67:17:24.7	328.2×236.4 (± 29.4)	79.57×57.33 (± 7.12)	26.3
MCSNR J0527–7134	05:27:50.02	-71:34:10.4	183.6×152.4 (± 14.4)	44.52×36.98 (± 3.55)	0.7

Table 7. Optical line intensities and ratios for extracted from the apertures of Fields 1 and 2 of MCSNR J0512–6717. The aperture positions are shown in Fig. 15. All fluxes are in units of erg cm $^{-2}$ s $^{-1}$ Å $^{-1}$. Dispersion errors are as in Dopita et al. (2007, 2010); Childress et al. (2014). The [N II] and [S II] ratios relative to H α correspond to the summation of their doublet lines. The last column shows the electron density (n_e) derived from the [S II] ratio and the updated calibration curve of Proxauf et al. (2014) with LDL meaning n_e is in the low-density limit. The fainter [O III] $\lambda 4959\text{\AA}$ and [N II] $\lambda 6548\text{\AA}$ lines could not be measured in 2A, 2B, and 2C. To determine the [N II]/H α ratios in these cases we used the fact that this is set by atomic physics to be ~ 2.9 (Acker et al. 1989) and the measured [N II] $\lambda 6583\text{\AA}$ to determine the ratio.

Aper.	H β	[O III] $\lambda 4959\text{\AA}$	[O III] $\lambda 5007\text{\AA}$	H α	[N II] $\lambda 6548\text{\AA}$	[N II] $\lambda 6583\text{\AA}$	[S II] $\lambda 6716\text{\AA}$	[S II] $\lambda 6731\text{\AA}$	[N II]/H α	[S II]/H α	[S II] ratio	n_e (cm $^{-3}$)
1A	5.69e-15	4.03e-15	1.23e-14	1.50e-14	8.75e-16	3.02e-15	4.85e-15	3.47e-15	0.26	0.55	1.40	55.2
1B	4.05e-15	4.54e-15	1.40e-14	1.24e-14	6.07e-16	1.68e-15	2.60e-15	1.82e-15	0.18	0.36	1.43	LDL
1C	3.18e-15	2.94e-15	8.82e-15	9.95e-15	4.47e-16	1.47e-15	2.54e-15	1.78e-15	0.19	0.43	1.43	LDL
1D	4.83e-15	4.28e-15	1.28e-14	1.62e-14	8.76e-16	2.68e-15	4.06e-15	2.83e-15	0.22	0.43	1.44	LDL
1E	2.82e-15	2.13e-15	6.36e-15	1.09e-14	6.65e-16	1.90e-15	3.84e-15	2.82e-15	0.24	0.61	1.36	74.6
2A	3.84e-16	–	–	1.27e-15	2.49e-16	1.82e-16	3.57e-16	2.59e-16	0.45	0.49	1.38	65.0
2B	2.95e-16	–	5.76e-16	1.18e-15	3.68e-17	1.81e-16	2.82e-16	2.36e-16	0.24	0.44	1.19	210.8
2C	1.07e-15	–	–	2.96e-15	4.09e-16	5.51e-16	1.08e-15	8.21e-16	0.43	0.64	1.32	102.6
2D	8.50e-16	3.81e-16	1.28e-15	2.45e-15	1.93e-16	4.28e-16	9.16e-16	7.19e-16	0.25	0.67	1.27	134.5
2E	1.22e-15	8.44e-16	2.29e-15	3.95e-15	1.74e-16	8.83e-16	1.54e-15	1.24e-15	0.27	0.70	1.25	159.0

shell vpshock model to the LMC abundance. The shell plus pure-Fe model improved the fit with $\chi^2_{\nu} = 1.20$, the results of which are given in Table 4. We also tried fitting an additional pure-O component, which gave the same $\chi^2_{\nu} = 1.20$ (Table 4 and Fig. 12).

The detection of extended X-ray emission and significant optical emission with [S II]/H α > 0.4 confirmed this object as an SNR.

4.2.6 MCSNR J0510–6708

The candidate SNR 0510–6708 was classified as such as it exhibited optical emission with a [S II]/H α > 0.4, indicative of an SNR. Radio-continuum emission was found to be centrally peaked but very weak with a flux density of 2.5 mJy at 1377 MHz (Bozzetto et al. 2017). The multi-wavelength images of MCSNR J0510–6708 are shown in Fig. 8. The multi-wavelength morphology of this ob-

ject is somewhat puzzling. There is a large, circular optical shell in the MCELS image, bright in both H α and [S II], but this does not show [S II]/H α > 0.4, and is therefore inconsistent with an SNR origin. In addition, the X-ray emission is not correlated with this large, circular shell, but projected outside the northwestern shell (Fig. 8 top-right) and is quite faint. Interestingly, there are regions with [S II]/H α > 0.4 which surround the X-ray emission (Fig. 8 bottom-left) and follow a different morphology than the large, circular shell. The 24 μm image shows a quite complex density structure and suggests that foreground absorption may play a significant role in the observed morphology. To investigate this further we compared the observed optical and X-ray morphologies to the HI and CO maps of Kim et al. (2003) and Fukui et al. (2008), respectively, shown in Fig. 19. From the HI contours, we expected the foreground N_{H} value be 2×10^{22} cm $^{-2}$ at most. However, this was determined to be

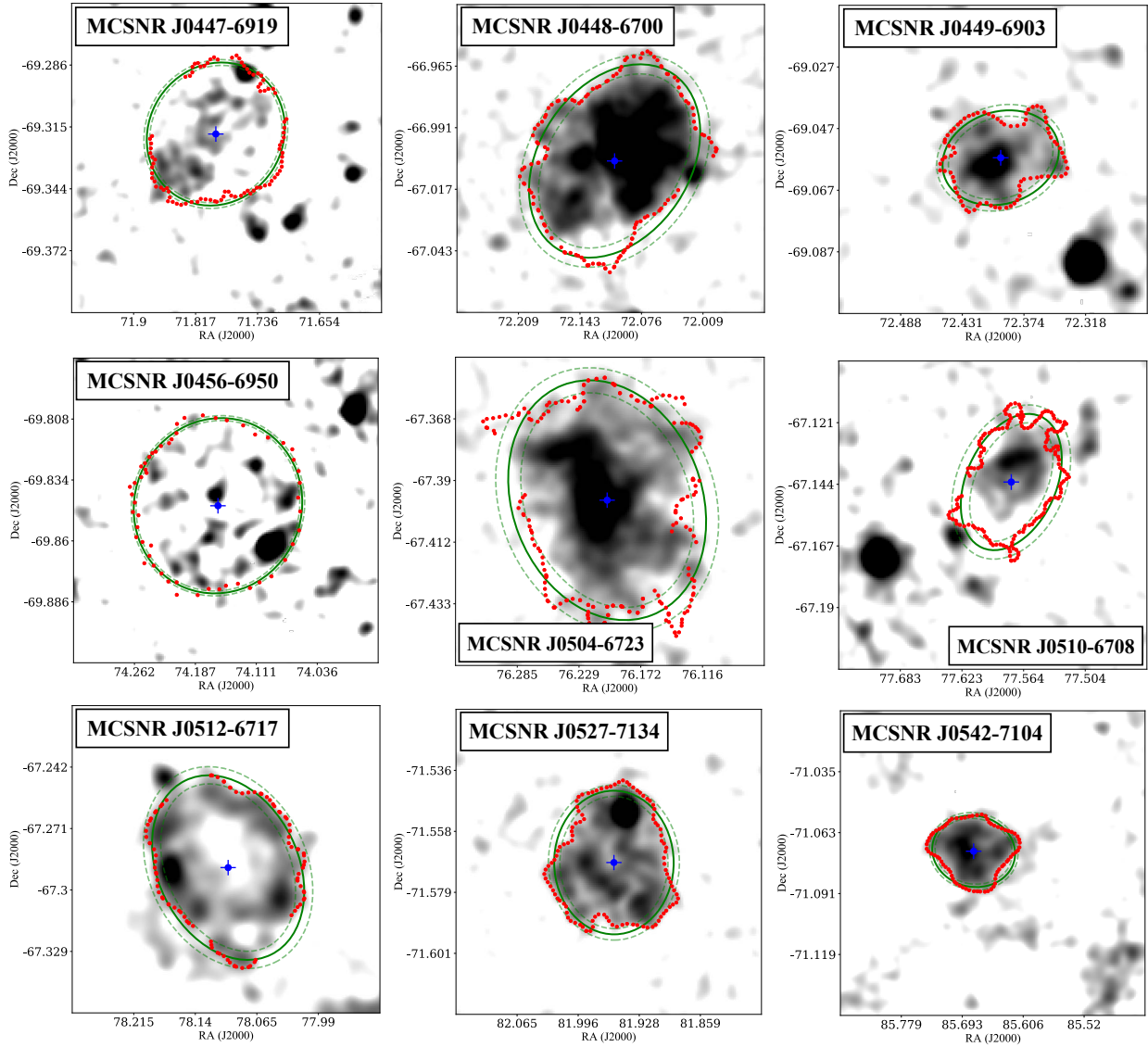


Figure 14. *XMM-Newton* EPIC images of each of our new SNRs with the best fit dimensions. The red points delineate the contour level used in the fits (see Sect. 3.4). The green solid line shows the best-fit ellipse to the contour, with the dashed lines indicating the 1σ error on the fit. The blue plus-sign marks the best-fit centre of the SNRs. See Sect. 4 for details on individual fits.

$\gtrsim 3 \times 10^{22} \text{ cm}^{-2}$ in our X-ray spectral fits, which suggests some additional absorption. The NANTEN map suggests that some molecular material could also be absorbing the X-ray emission in the east and south of the remnant. In any case, the fitted N_{H} is sufficient to mask out any faint soft emission that could come from the south-east region and/or inside the large, circular optical shell so the observed X-ray morphology could be due to absorption effects.

The location of the X-ray emission and the extent of the $[\text{S II}]/\text{H}\alpha$ contour outside of the large, circular shell suggests that either we are seeing an SNR projected against a stellar wind bubble or superbubble, or that an SN has occurred near the bubble or superbubble shell and blown out into the surroundings. We determined the position and size of the remnant using the $[\text{S II}]/\text{H}\alpha=0.4$ contour, with the results shown in Table 6 and shown in Fig. 14. The size was found to be $29.46 \times 47.03 (\pm 5.92)$ pc, which is consistent with evolved SNRs in the LMC.

The X-ray emission detected in MCSNR J0510–6708 is rather

faint. Due to the low number of counts in the MOS1 and MOS2 spectra, we consider the pn spectrum only. We initially fitted the X-ray emission using the *vpshock* model, however, we could not constrain the ionisation parameter with only a lower limit of $\gtrsim 10^{10} \text{ cm s}^{-3}$ found. We therefore assumed CIE and fixed the parameter to $10^{12} \text{ cm s}^{-3}$. This provided a good fit to the data ($\chi^2_{\nu} = 1.01$) and constraints on the free parameters (see Table. 3). We also tried fits with some abundances allowed to vary, however, these did not provide constraints on the parameters. This is not surprising given the low number of counts and degrees of freedom.

Given that the extended X-ray emission appears to be associated with enhanced $[\text{S II}]$ and not the large optical shell, we confirmed this object as an SNR.

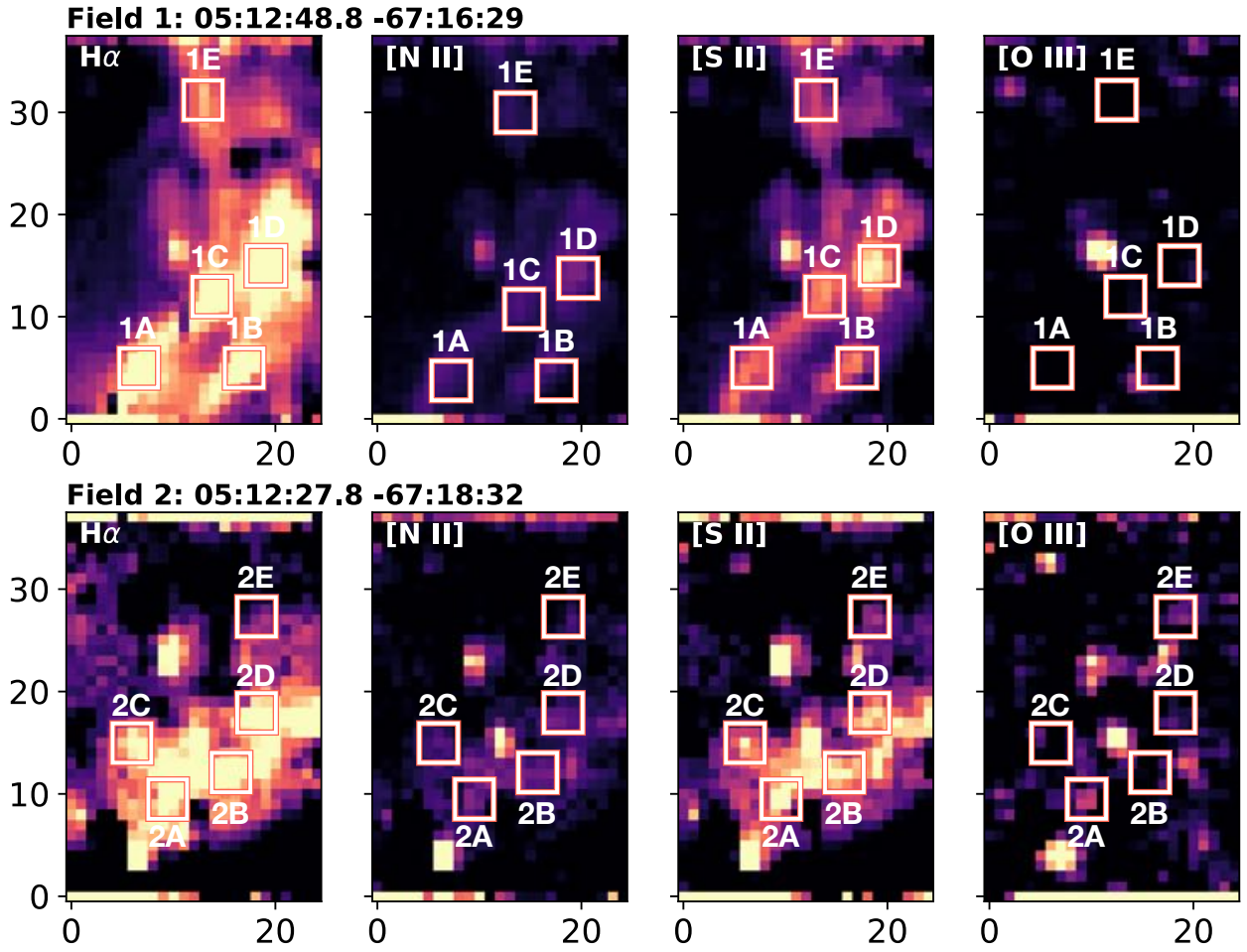


Figure 15. Emission line images produced by collapsing sub-cubes extracted from around $H\alpha$, the $[S\ II]\lambda 6716\text{\AA}, \lambda 6731\text{\AA}$ doublet, $[N\ II]\lambda 6583\text{\AA}$, and $[O\ III]\lambda 5007\text{\AA}$. The fields and species are indicated in the panels. Also shown are the $4'' \times 4''$ apertures used for spectral extraction. The color scale is linear and the scale limits for each field are the same.

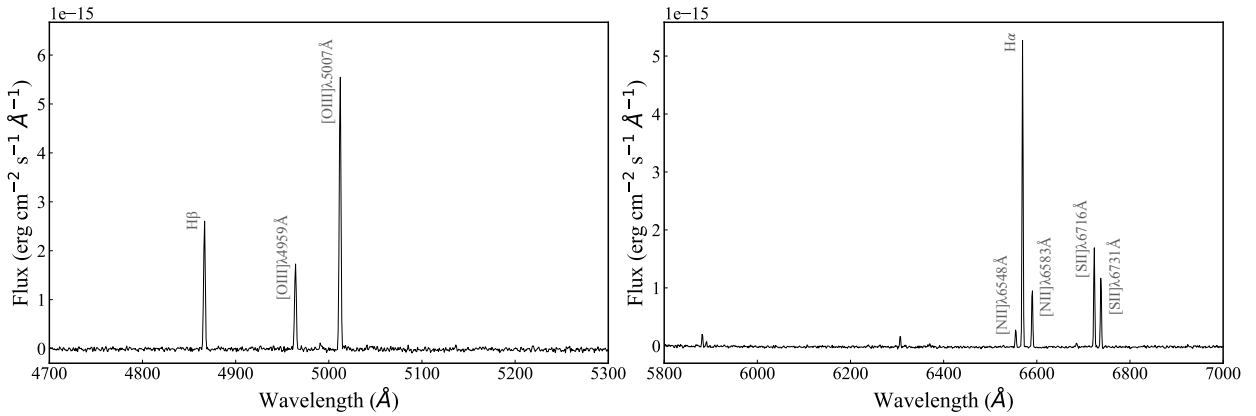


Figure 16. Continuum subtracted blue (left) and red (right) spectra from extraction aperture 1A (see Fig. 15). The observed emission lines are indicated on the plot.

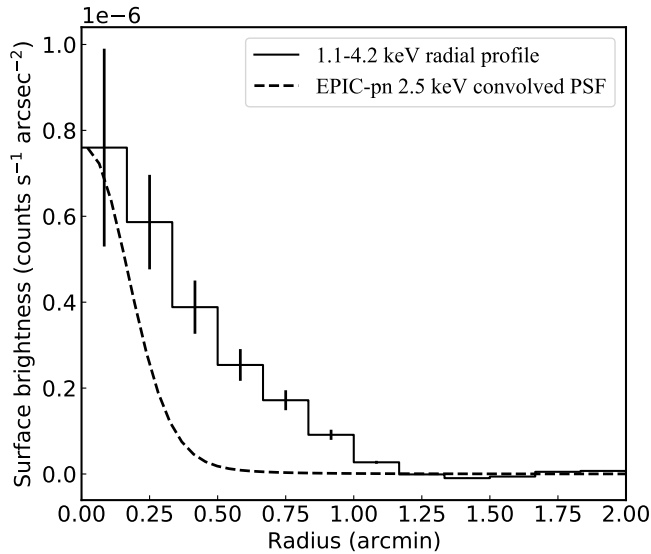


Figure 17. Radial profile plot of the hard emission in MCSNR J0449-6903, extracted from the 1.1–4.2 keV image, centred on the brightest emission region, and in $10''$ bins. The dashed line shows the EPIC-pn PSF at 2.5 keV for comparison (see text) which has been scaled to the peak of the radial profile.

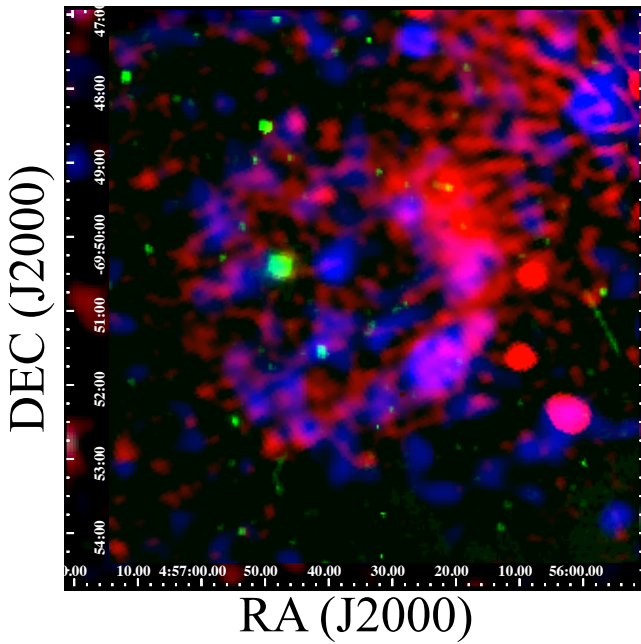


Figure 18. False color image of MCSNR J0456-6950 with RGB=ASKAP 888 MHz, $H\alpha$, 0.3–0.7 keV. The ASKAP image reveals a large circular shell coincident with the faint X-ray emission.

4.2.7 MCSNR J0512–6717

This object was detected serendipitously in an *XMM-Newton* observation of another candidate, and subsequently confirmed SNR, MCSNR J0512–6707 (Kavanagh et al. 2015b). Located in the south of the FOV, 0512–6717 presented a large circular morphology in soft X-rays. Faint 20 cm radio continuum emission was detected along

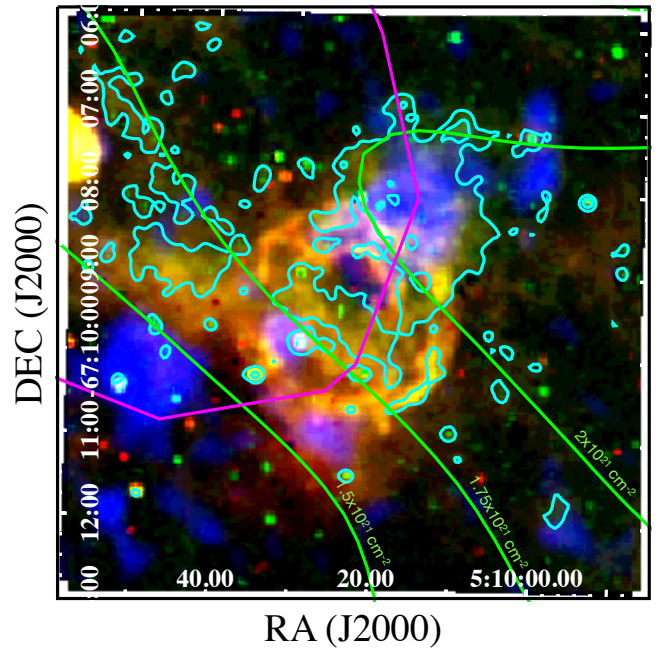


Figure 19. False color image of MCSNR J0510–6708 with RGB= $H\alpha$, [S II], 0.7–1.1 keV. The cyan contour represents [S II]/ $H\alpha > 0.4$ (see Fig. 8). The green contours represent HI and are shown in equivalent hydrogen column (N_H) which were derived from the HI maps of Kim et al. (2003). The magenta contour is 1σ level of the 12CO ($J=1-0$) line observed with the NANTEN telescope (Fukui et al. 2008).

the western side of the object (Bozzetto et al. 2017, their Fig. 2, middle-left), though it was not possible to construct a radio continuum spectral energy distribution and estimate the spectral index. Therefore, this object was classed as a candidate in Bozzetto et al. (2017). The multi-wavelength images of this object are shown in Fig. 9. Extended X-ray emission was detected in a distinct shell-like morphology. The optical emission line images of the object did not show any morphological consistency with the X-ray shell with some regions of [S II]/ $H\alpha > 0.4$ that were not coincident with the X-ray emission. Interestingly, the [S II]/ $H\alpha$ image reveals a shell-like region with [S II]/ $H\alpha > 0.4$ of similar size to the X-ray shell but shifted northwards. It is unclear if this is related to the X-ray shell with the observed displacement being due to a projection effect. To confirm the SNR nature of the object, we performed follow-up optical spectroscopic observations on regions of the X-ray shell that showed clearly enhanced and filamentary [S II] emission. The spectral analysis, described in Sect. 3.5, showed that the optical emission in these regions was consistent with an SNR origin with [S II]/ $H\alpha > 0.4$ (see Table 7). The $24 \mu\text{m}$ image shows an inhomogeneous ambient density surrounding the SNR though this does not appear to have significant influence on the X-ray or optical morphologies. We fitted the 0.3–0.7 keV X-ray contour of MCSNR J0512–6717 to determine a size of $57.33 \times 79.57 (\pm 7.12)$ pc (see Table 6 and Fig. 14) which suggests an evolved SNR.

We tried to fit the X-ray emission from MCSNR J0512–6717 using the vps shock model. However, the resulting fit could not constrain abundance parameters or the ionisation timescale. Given the large size of the object, we assumed that the plasma has most likely reached CIE and so fixed the ionisation timescale to $10^{12} \text{ cm s}^{-3}$. Trial fits with elemental abundances allowed to vary showed that

constraints could be placed on O and Fe abundances. This model provided an acceptable fit ($\chi^2_{\nu} = 1.14$, see Table 3). The best fit temperature of 0.19 (0.18–0.21) keV is consistent with an evolved SNR and the fitted abundances are consistent with those in the swept-up ISM in other LMC SNRs (e.g. Maggi et al. 2016, their Table 5).

Based on the detection of extended thermal X-ray emission and optical signatures of an SNR, including $[S\ II]/H\alpha > 0.4$, we confirmed this object as an SNR.

4.2.8 MCSNR J0527–7134

Radio continuum emission was detected from the candidate 0527–7134 at 20 cm and 36 cm with a shell-like morphology that is correlated with an $[S\ II]$ dominated optical shell (Bozzetto et al. 2017, their Fig. 2, bottom-right). The enhanced $[S\ II]$ optical shell and determined spectral index $\alpha = -0.52$ both indicated an SNR nature for the object. Our multi-wavelength images are shown in Fig. 10. Soft extended X-ray emission is clearly detected and associated with a significant $[S\ II]$ enhancement with $[S\ II]/H\alpha > 0.4$. The X-ray and enhanced $[S\ II]$ emission are very well correlated and suggest an obvious association. A very slight ambient density gradient is apparent in the 24 μm image, though this appears to have little influence on the optical or X-ray morphology. We used the outer 0.3–0.7 keV contour to determine the position and size of the remnant, given in Table 6 and shown in Fig. 14. The size was found to be $36.98 \times 44.52 (\pm 3.55)$ pc, typical of an evolved LMC SNR.

We fitted the X-ray emission from MCSNR J0527–7134 using the vpshock model allowing the abundances of O and Ne to vary, and all others fixed to the LMC abundance. Trial fits with other elemental abundances free did not allow for constraints on the parameters. This model provided a good fit to the data with $\chi^2_{\nu} = 0.97$ (see Table 3). However, some parameters were not well constrained, i.e. $kT = 0.53$ (0.19–1.32) keV and $\tau = 0.26$ (0.09–12.66) 10^{11} s cm^{-3} . Since the low and high 90% confidence limit on kT and τ , respectively, are consistent with an evolved SNR, we also assumed that the plasma was in CIE and ran a trial fit with τ fixed to 10^{12} cm^{-3} , which is shown in Table 3. The CIE model also provided a good fit to the data with $\chi^2_{\nu} = 0.98$ (see Table 3), with tighter constraints on the plasma temperature (kT 0.19 (0.19 – 0.21) keV). In both models, the fitted abundances of O and Ne are consistent with those in the swept-up ISM in other LMC SNRs (e.g. Maggi et al. 2016, their Table 5). The interpretation of the results of both fits are discussed in more detail in Sect. 5.2.4 where SNR properties are derived using the Sedov evolutionary model.

Based on the detection of extended thermal X-ray emission, correlated $[S\ II]/H\alpha > 0.4$, and the previously reported non-thermal radio emission (Bozzetto et al. 2017), we confirmed this object as an SNR.

4.2.9 MCSNR J0542–7104

The candidate 0542–7104 showed a shell-like optical emission with enhanced $[S\ II]$. Radio emission was also detected at the brightest region of $[S\ II]$ emission with a possible correlation to the X-ray source [HP99] 1235 (Bozzetto et al. 2017). Recently, this object was confirmed as an SNR by Yew et al. (2021) based on its optical spectrum. They measured a size of 73×51 pc for the optical shell. Our multi-wavelength images of MCSNR J0542–7104 are shown in Fig. 11, with the $[S\ II]/H\alpha$ contours from Yew et al. (2021). Extended X-ray emission, primarily in the 0.7–1.1 keV range, is detected towards the centre of the optical shell. Similar morphology has been observed in, e.g. MCSNR J0508–6830, MCSNR J0511–6759 (Maggi

et al. 2014), and MCSNR J0527–7104 (Kavanagh et al. 2016) and suggests that this SNR belongs to the class of evolved SNRs with enhanced Fe emission, similar to MCSNR J0504–6723 discussed above. The observed Fe-rich core morphology has been interpreted as the X-ray emission from the shocked ISM being too faint to detect whereas the hot Fe gas in the core remains detectable. We used the 0.7–1.1 keV contour to determine the size of the core emission region to be $33.46 \times 28.57 (\pm 2.29)$ pc (see Fig. 14). Knots of emission are also observed outside the core to the south, similar to MCSNR J0511–6759. Maggi et al. (2014) interpret these features being clumps of X-ray emitting ejecta shrapnel. There appears to be a marginal ambient density gradient in the 24 μm image in the northeast-southwest direction. However, the optical shell is brighter and fainter in the lower and higher density regions, respectively. If indeed the western shell is evolving into a higher density region, we would expect the optical emission to be brighter in the west. For this reason, it is likely the density gradient is a projection effect and does not represent the real ambient conditions of the SNR.

To demonstrate the overabundance of Fe in the core we fitted the X-ray spectrum with the vpshock model, allowing the Fe abundance to vary, resulting in a best fit abundance of $(Z/Z_{\odot})_{\text{Fe}} \gtrsim 2$ and a high $kT \gtrsim 0.5$ keV for a $\chi^2_{\nu} = 1.21$. As with MCSNR J0504–6723, we also tried freeing Ne on its own and in combination with Fe. The fit with Ne free resulted in a poorer fit with $\chi^2_{\nu} = 1.35$. Freeing both Ne and Fe resulted in a similarly good fit as with only Fe free ($\chi^2_{\nu} = 1.20$) though neither abundance was well constrained but the Fe was clearly enhanced $(Z/Z_{\odot})_{\text{Fe}} \gtrsim 1.5$ while the lower limit of the Ne abundance was consistent with the LMC value. For this reason, we proceed under the assumption that the emission is Fe dominated.

We then took the same approach for other similar objects, including MCSNR J0504–6723 in this work, of fitting the core emission with spectral components comprising pure Fe, and possibly O (e.g. Maggi et al. 2014, 2016; Kavanagh et al. 2016). We initially allowed the ionisation timescale to vary, however we could not constrain this parameter so instead fixed it to 10^{12} cm^{-3} . We first tried a pure Fe only model which provided a reasonable fit to the data ($\chi^2_{\nu} = 1.25$, see Table 4). However, there were clearly residuals between 0.5–0.6 keV. For this reason we added a pure O component. Even though type Ia SNe can produce little O, its mass fraction could be as much as $\sim 30\%$ ($\sim 0.3 M_{\odot}$) if most of the outer ejecta layers consist of O (see, e.g. Kosenko et al. 2010, and references therein). For low plasma temperatures (< 1 keV), the emissivity of the O VII and O VIII lines is high, leading to significant line emission in the 0.5–0.6 keV range. We initially linked the Fe and O plasma temperatures, which is expected if the Fe and O are co-spatial and the plasmas have reached CIE. However, this did not properly account for the residuals in the 0.5–0.6 keV range ($\chi^2_{\nu} = 1.22$, see Table 4). We therefore allowed the O plasma temperature to vary independently from Fe. This provided a much improved fit to the data ($\chi^2_{\nu} = 1.02$, see Table 4 and Fig. 12). The different values of kT for the Fe (0.58 (0.54 – 0.62) keV) and O (0.19 (0.14 – 0.24) keV) components suggested these plasmas are not co-spatial.

5 DISCUSSION

5.1 SNR evolutionary properties

The X-ray spectral models for several of our SNRs contained a soft thermal component interpreted as emission from an evolving Sedov-phase shell. We estimated the physical properties of these SNRs using the Sedov dynamical model and the SNR dimensions determined

in Sect. 3.4 where we assumed that the measured semi-major and semi-minor axes of each of our objects were the first and second semi-principal axes of an ellipsoid, and that the third semi-principal axis was in the range between the two. The following procedure has been used previously in, e.g. Sasaki et al. (2004); Kavanagh et al. (2015b); Maggi et al. (2016); Kavanagh et al. (2016). However, we reiterate the procedure here and introduce an additional term representing the hot gas filling factor to convey how our derived SNR properties may vary depending on this term.

From our estimates on the dimensions of the SNRs, we determined their volume (V) limits and corresponding effective radii (R_{eff}). The best fit shell X-ray temperatures determined in our spectral fits (see Tables 3, 4, 5) correspond to a shock velocity

$$v_s = \left(\frac{16kT_s}{3\mu} \right)^{0.5}, \quad (1)$$

where kT_s is the post-shock temperature and μ is the mean mass per free particle which, for a fully ionised plasma with LMC abundances, is $\mu = 0.61m_p$. The ages of our SNRs were then determined using the Sedov solution:

$$v_s = \frac{2R}{5t}, \quad (2)$$

where $R = R_{\text{eff}}$ and t is the age of the remnant. The pre-shock H densities ($n_{\text{H},0}$) in front of the blast wave of each SNR were then determined from the emission measure (EM , see Tables 3, 4, 5). An expression for the emission measure can be determined by evaluating the emission integral over the Sedov solution using the approximation for the radial density distribution of Kahn (1975), which gives

$$\int n_e n_{\text{H}} dV = EM = 2.07 \left(\frac{n_e}{n_{\text{H}}} \right) n_{\text{H},0}^2 V f, \quad (3)$$

where n_e and n_{H} are electron and hydrogen densities, respectively, V is the volume (e.g., Hamilton et al. 1983), f is a filling factor, and $n_e/n_{\text{H}} = 1.21$. We then estimated the pre-shock density from $n_0 \sim 1.1n_{\text{H},0}$. The initial explosion kinetic energies (E_0) were determined from the equation:

$$R = \left(\frac{2.02E_0 t^2}{\mu_n n_0 f^{-1/2}} \right)^{1/5}, \quad (4)$$

where μ_n is the mean mass per nucleus ($=1.4m_p$). The swept-up masses contained in the shell of each SNR is given by $M = V\mu_n n_0 f^{1/2}$. The determined properties for each SNR are listed in Table 8 for an assumed $f = 1$.

5.2 Typical Sedov-phase SNRs

5.2.1 MCSNR J0448–6700

The multi-wavelength properties of MCSNR J0448–6700 suggested either an SNR evolving into an ambient density gradient or that the SN progenitor had a significant proper motion in an approximate east-to-west direction (see Sect. 4.2.2). The size was found to be $55.54 \times 77.32 (\pm 7.15)$ pc, which is consistent with large evolved SNRs in the LMC, which is further supported by the X-ray spectrum being consistent with a cool thermal plasma ($kT \sim 0.2$ keV) in CIE. From the spectral fit results and size estimate, we determined that this SNR is consistent with the Sedov dynamical model with an initial explosion energy in the range $(0.24 - 2.06) \times 10^{51}$ erg and age of 27–35 kyr (see Table 8).

5.2.2 MCSNR J0456–6950

MCSNR J0456–6950 was found to have an X-ray faint shell without marginal evidence for an optical counterpart along the south of the shell. However, the ASKAP 888 MHz image (see Fig. 18) revealed a large circular shell which led us to confirm this object as an SNR (Sect. 4.2.4). The size was found to be $65.80 \times 62.26 (\pm 1.80)$ pc and the X-ray spectrum was consistent with a soft thermal plasma ($kT \sim 0.15$ keV) in CIE. Comparison with the Sedov dynamical model shows an underestimate of the explosion energy $(0.10 - 0.27) \times 10^{51}$ erg (see Table 8). This could be due to the assumed filling factor of unity. If $f < 1$, the determined explosion energy would be higher (see Eq. 4). The estimated age from the Sedov model was 34–40 kyr.

5.2.3 MCSNR J0512–6717

Our multi-wavelength study of MCSNR J0512–6717 revealed a large evolved SNR with a distinct ring-like morphology in X-rays. Its size was found to be $57.33 \times 79.57 (\pm 7.12)$ pc, which is consistent with large evolved SNRs in the LMC. Its X-ray spectrum was best described with a soft thermal plasma ($kT \sim 0.2$ keV) in CIE (Sect. 4.2.7). From the spectral fit results and size determination, we found that MCSNR J0512–6717 is consistent with the Sedov dynamical model with an initial explosion energy in the range $(0.21 - 1.75) \times 10^{51}$ erg and age of 28–36 kyr (see Table 8).

5.2.4 MCSNR J0527–7134

The multi-wavelength morphological study of MCSNR J0527–7134 revealed a bright and uniform X-ray shell, which was significantly correlated with the [S II]/H α morphology. The size was found to be $36.98 \times 44.52 (\pm 3.55)$ pc, typical of an evolved LMC SNR. Its X-ray spectrum could be described with either a CIE or NEI thermal plasma model. However, the NEI model was not as well constrained as the CIE model (Sect. 4.2.8) but both are consistent with a plasma CIE. From the spectral fit results and size determination, we found that MCSNR J0527–7134 is consistent with the Sedov dynamical model with an initial explosion energy in the range $(0.02 - 1.32) \times 10^{51}$ erg and age of 7–21 kyr (see Table 8).

5.3 Evolved Fe-rich SNRs

We have identified two of our sample as new members of the class of evolved SNRs with Fe-rich interiors, bringing the total number to 13. The members of this class are listed in Table 9.

The X-ray spectral models for MCSNR J0504–6723 and MCSNR J0542–7104 contained pure Fe and O components representing hot ejecta. We estimated various properties of the ejecta following the method described in detail in, e.g., Kosenko et al. (2010); Bozzetto et al. (2014); Maggi et al. (2014); Kavanagh et al. (2016). For a Type Ia explosion, we would expect that about half of the ejecta mass is Fe, $\sim 0.7 M_{\odot}$ (e.g. Iwamoto et al. 1999) and can be determined from the emission measure of the ejecta components and the volume they occupy. The Fe mass given by the equation

$$M_{\text{Fe}} = (V_{\text{Fe}} EM_{\text{Fe}})^{0.5} (n_e/n_{\text{Fe}})^{-0.5} m_{\text{U}} A_{\text{Fe}}, \quad (5)$$

where V_{Fe} is the volume of the Fe, $EM_{\text{Fe}} = n_e n_{\text{Fe}} V$ is the emission measure of the Fe gas, n_e/n_{Fe} is the electron to Fe-ion ratio, m_{U} is the atomic mass unit, and A_{Fe} is the atomic mass of Fe. EM_{Fe} is obtained from the normalisation of the Fe component and is listed in Table 4.

Table 8. Derived properties of our SNR sample. All quoted values assume a filling factor f of unity.

Name	n_0 ($f^{-1/2}10^{-2} \text{ cm}^{-3}$)	v_s (km s^{-1})	Age (kyr)	M ($f^{1/2} M_\odot$)	E_0 ($f^{-1/2}10^{51} \text{ erg}$)
MCSNR J0447–6919	2.5–6.3	409–501	22–28	78–230	0.17–0.95
MCSNR J0448–6700	4.4–8.8	388–419	27–35	157–550	0.24–2.06
MCSNR J0449–6903	1.6–4.4	419–572	9–15	6–25	0.01–0.17
MCSNR J0456–6950	1.6–2.6	317–366	34–40	71–129	0.10–0.27
MCSNR J0504–6723	0.6–1.8	399–755	15–35	22–115	0.04–1.35
MCSNR J0510–6708	2.3–23.0	366–518	12–22	12–270	0.01–1.82
MCSNR J0512–6717	3.4–6.9	388–419	28–36	134–470	0.21–1.75
MCSNR J0527–7134	1.2–4.5	399–1051	7–21	12–64	0.02–1.32

Table 9. Evolved Fe-rich SNRs in the LMC.

Names (MCSNR)	Reference
J0504–6723, J0542–7014	this work, Yew et al. (2021)
J0506–7025, J0527–7104	Kavanagh et al. (2016)
J0508–6830, J0511–6759	Maggi et al. (2014)
J0508–6902	Bozzetto et al. (2014)
J0454–6713	Seward et al. (2006)
J0534–7033, J0536–7039	Borkowski et al. (2006)
J0547–6941	Williams et al. (2005)
J0547–7025, J0534–6955	Hendrick et al. (2003)

The $n_{\text{Fe}}/n_{\text{H}}$ value is calculated from the Fe abundance parameter of the model. There are two limiting cases for the value of the n_e/n_{Fe} ratio as the number of free electrons n_e is dependent on the amount of H in the ejecta (Hughes et al. 2003). If there is no H then n_e/n_{Fe} only depends on the average ionisation state of the Fe, taken as 18.3 (Shull & van Steenberg 1982). Conversely, if a similar mass of H is mixed into the Fe-rich ejecta, the number density of Fe over H is 1/56, and n_e/n_{Fe} is 74.3.

We estimated the volume range occupied by the Fe-rich plasmas in our objects by assuming that they are ellipsoidal. We fitted ellipses to the emission regions, measured the semi-major and semi-minor axes, and determined a volume range assuming that the third semi-axis was equal to either the semi-major or semi-minor axes. We must also consider whether or not the ejecta are clumpy. In this case, the emitting volume must be modified by a filling factor of ~ 0.4 (see Kosenko et al. 2010, and references therein), in which case the Fe content reduces by a factor of $\sqrt{0.4} \approx 0.63$.

5.3.1 MCSNR J0504–6723

The multi-wavelength images of MCSNR J0504–6723 showed an SNR which is elongated in a southwest-northeast direction. The X-ray morphology was notable because of the bright and central 0.7–1.1 keV emission surrounded by the softer 0.3–0.7 keV, suggesting that MCSNR J0504–6723 belongs the class of evolved SNRs with enhanced Fe emission. The associated optical emission has an unusual morphology, appearing more rectangular than circular, most likely because of ambient density variations revealed in the 24 μm image. The size was found to be $58.00 \times 75.62 (\pm 7.71)$ pc, which is consistent with evolved SNRs in the LMC. The shell component was best fitted with a soft thermal plasma ($kT \sim 0.2$ keV) in CIE (Sect. 4.2.5). From the spectral fit results and size estimate, we determined that the SNR shell is consistent with the Sedov dynamical model with an initial explosion energy in the range $(0.04 - 1.35) \times 10^{51}$ erg and age of 15–35 kyr (see Table 8).

For the central Fe-rich plasma, the determination of V_{Fe} presents

a similar problem to MCSNR J0506–7025 (Kavanagh et al. 2016), namely that the emission in the 0.7–1.1 keV range, where the Fe-L shell lines dominate, is not confined to a well-defined core. While there does appear to be an aggregate of Fe-L shell emission near the SNR centre, there are extensions protruding to the north east and south. It is unclear if these extensions are due to the Fe-rich ejecta or to enhancements in the shell emission.

As for MCSNR J0506–7025 in Kavanagh et al. (2016), we created an X-ray colour map to gauge the distribution of Fe-rich plasma in the core of MCSNR J0504–6723. We used the same two energy bands, a soft band $S = 0.3\text{--}0.7$ keV (where the shell dominates) and a hard band $H = 0.7\text{--}1.1$ keV (where the Fe L-shell bump peaks), and the colour S/H is then given by $N_{0.3\text{--}0.7 \text{ keV}}/N_{0.7\text{--}1.0 \text{ keV}}$. As in Kavanagh et al. (2016), we binned the combined 0.3–1.1 keV image using Voronoi tessellation to achieve a minimum signal-to-noise ratio per bin but in this case used the VorBin python package which is an implementation of the Cappellari & Copin (2003) Voronoi binning algorithm, with the weighted Voronoi tessellation option (Diehl & Statler 2006) set. We found that a signal-to-noise of 10 gave a useful estimate of S/H in each bin while producing small enough bins to adequately trace the Fe distribution in MCSNR J0504–6723. We then used the tessellates defined for the 0.3–1.1 keV image to bin the S and H images, and calculated S/H , which is shown in Fig. 20. A threshold level to separate Fe-L shell dominated regions from the shell regions was still needed. Again we employed the method of Kavanagh et al. (2016) of performing spectral simulations assuming that the best-fit core and shell component parameters are constant over the remnant, allowing only the relative normalisation between the shell and core components to vary. These simulations suggested a threshold of ~ 0.7 , with values below this corresponding to Fe L-shell dominated regions. We defined a contour at this threshold (see Fig. 20) which showed that the Fe emission is non-uniformly distributed, with a narrow extension towards the north east, and a non-contiguous morphology in the south. Given such an inhomogeneous morphology, it is difficult to obtain an estimate of V_{Fe} . Nevertheless, we attempted to determine the volume of the Fe-rich core by fitting an ellipse by eye around the inner two contours in Fig. 20. We estimate this core region to have a size of 26.76×51.78 pc which results in a volume estimate of $V_{\text{Fe}} = 0.57 - 1.10 \times 10^{60} \text{ cm}^3$. We used this in Eq. 5 to determine an Fe mass of 2.3–3.8 M_\odot for a pure metal plasma with no H and a filling factor of 1, and 1.1–1.8 M_\odot in the case of an equivalent mass of H is mixed into the Fe-rich ejecta. Assuming a clumpy ejecta leads to Fe masses of 1.4–2.4 M_\odot and 0.7–1.1 M_\odot for a pure metal plasma with no H and with equivalent amount of H mixed into the Fe-rich ejecta, respectively. These results indicate that a clumpy ejecta with an admixture of H of similar mass to the Fe ejecta is required for agreement between our determined Fe mass and that expected from Type Ia explosive nucle-

osynthesis yields (e.g. [Iwamoto et al. 1999](#)), though note that this conclusion is still reliant on our coarse V_{Fe} estimate.

5.3.2 MCSNR J0542–7104

Both the X-ray morphology and spectral composition of MCSNR J0542–7104 indicated that the emission is primarily from Fe-rich ejecta. Unlike MCSNR J0504–6723, the morphology of the core is much more regular, being approximately circular. We used the size of the core region determined in Sect. 4.2.9 to estimate the ejecta volume to be $V_{\text{Fe}} = 4.30 - 4.92 \times 10^{59} \text{ cm}^3$. We used this in Eq. 5 and a filling factor of 1 to determine Fe masses of 1.9–2.5 M_{\odot} and 0.9–1.3 M_{\odot} for the cases of no H and an equivalent mass of H mixed into the Fe-rich ejecta, respectively. Assuming a clumpy ejecta leads to corresponding Fe masses of 1.2–1.6 M_{\odot} for the no H and 0.6–0.8 M_{\odot} for the equivalent amount of H. These results again indicate that a clumpy ejecta with an admixture of H of similar mass to the Fe ejecta is required for agreement between our determined Fe mass and that expected from Type Ia explosive nucleosynthesis yields (e.g. [Iwamoto et al. 1999](#)).

5.4 Other SNRs

Three of our SNR sample can not be considered either typical Sedov-phase or Fe-rich SNRs because of their unusual morphologies and/or spectra. These are discussed in the following subsections.

5.4.1 MCSNR J0447–6919

The multi-wavelength images of MCSNR J0447–6919 showed a large optical shell with faint X-ray emission distributed between the

eastern and western shells, elongated in a southeast-northwest direction. Morphologically, this is similar to MCSNR J0527–7104 in which the X-ray emission is primarily due to Fe ejecta ([Kavanagh et al. 2016](#)). Because of the faintness of the X-ray emission in MCSNR J0447–6919, we could only fit simple models to the spectrum (see Sect. 4.2.1). Despite the lack of a clear Fe L-shell hump as in the Fe-rich SNRs in our sample, the best fit was provided by a CIE plasma with free Fe abundance, suggesting that the X-ray emission may indeed be due to Fe-rich ejecta. Deeper observations of this object are required to better identify the spectral components. To determine the likely properties of this SNR, we assume the CIE model represents the SNR shell emission. With these results and the size estimate, we used the Sedov dynamical model to determine an initial explosion energy in the range $(0.17 - 0.95) \times 10^{51} \text{ erg}$ and age of 22–28 kyr. The explosion energy is lower than the canonical 10^{51} erg , which could result from our assumed filling factor of unity. If $f < 1$, the determined explosion energy would increase and be more consistent with the Sedov model. These, along with other properties, are listed in Table 8.

5.4.2 MCSNR J0449–6903

MCSNR J0449–6903 is perhaps the most puzzling object in our sample. As described in Sect. 4.2.3, the X-ray emission appears to originate from two distinct regions: a faint, soft shell consistent with an evolved SNR; and a harder core region. The core emission could be fitted equally well with either a thermal plasma or a non-thermal power-law model, though the model complexity and constraints provided by our fits are severely limited by the count statistics. The thermal interpretation yields a $kT=2.81$ (2.06–4.60) keV and suggests hotter ejecta emission but there is no evidence for enhanced abundances which should also be present if the emission is due to shock-heated ejecta. It is unclear as to what could be the origin of the emission in the non-thermal interpretation. The location of the hard emission at the centre of the remnant and its radius ($1.16 (\pm 0.08)'$, corresponding to $\sim 16.9 (\pm 1.1) \text{ pc}$ at the LMC distance, see Sect. 4.2.3) could point to a faint pulsar wind nebula (PWN) as has been observed in other LMC SNRs such as MCSNR J0453–6829 ([Haberl et al. 2012](#)) and the N 206 SNR ([Williams et al. 2005](#)), though the possible PWN in MCSNR J0449–6903 would be somewhat larger and fainter, e.g. the PWN in MCSNR J0453–6829 is less than half the size with $R \sim 7 \text{ pc}$ ([Gaensler et al. 2003](#)). The hard extended source is also larger than other well-known X-ray PWNe, e.g. the Crab ($R < 1 \text{ pc}$), 0540–69.3 ($R < 1 \text{ pc}$), G21.5–0.9 ($R \sim 3.5 \text{ pc}$), and 3C58 ($R < 5 \text{ pc}$) ([Petre et al. 2007](#), and references therein), though these are associated with younger SNRs. The extent of the hard source is even comparable to the size of MCSNR J0449–6903 itself (see Sect. 3.4 and Table 6). The radii of a PWNe will be closest to the host SNR shell at the end of the initial expansion phase ([Gelfand et al. 2009](#)). As described below, we estimated the age of the SNR to be 9–15 kyr and the ambient density to be $1.6\text{--}4.4 f^{-1/2} 10^{-2} \text{ cm}^{-3}$. From Fig. 2 of [Gelfand et al. \(2009\)](#), for a PWN-hosting SNR evolving into a similar low density medium, their respective radii will be at their closest point after $\sim 5 \text{ kyr}$, slightly less than the estimated age of MCSNR J0449–6903. If the hard extended source is a PWN, it is likely in the reverse shock collision and first compression phase. Deeper X-ray observations of this object are required to better constrain the properties of the hard source. In a multi-wavelength context, we would also expect the hard X-ray emission to be correlated with radio emission. [Bozzetto et al. \(2017\)](#) report on the radio emission from MCSNR J0449–6903. While they do detect radio emission inside the SNR, it is concentrated towards the western shell, offset

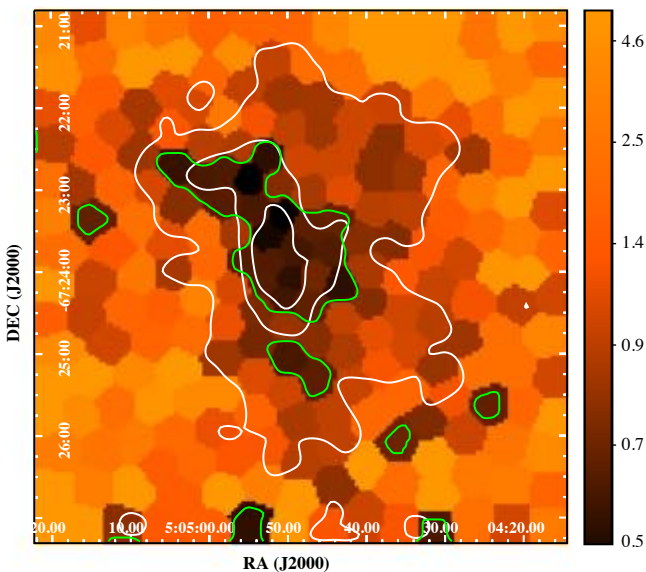


Figure 20. Adaptively binned X-ray colour map of MCSNR J0504–6723 using Voronoi tessellation. The tessellates are defined so that each has a S/N of 10. Lower values of S/H indicate higher contributions from Fe L-shell emission. The white contours show the 0.3–0.7 keV contours from Fig. 7-top right and the green contour outlines the Fe L-shell emission regions, set to $S/H < 0.7$ (see text).

from the hard X-ray emission (their Fig. 1, top right). Furthermore, the determined radio spectral index of $\alpha = -0.50 \pm 0.01$ is steeper than expected from a PWN, which should be flatter. The true origin of the hard X-ray emission remains unclear.

We assumed the soft component in our models represents emission from the expanding shell. Adopting the soft component parameters from the thermal plasma plus power law fit with the estimated size, we used the Sedov dynamical model to determine an initial explosion energy in the range $(0.01 - 0.17) \times 10^{51}$ erg and age of 9–15 kyr. The explosion energy is much lower than the canonical 10^{51} erg, which might be explained by the filling factor being set to unity. If $f < 1$, the determined explosion energy would increase and be more consistent with the Sedov model. These, along with other properties, are listed in Table 8.

5.4.3 MCSNR J0510–6708

The interpretation of the morphology of this object is complicated by the large, optical shell. As described in Sect. 4.2.6, the [S II]/H α contours indicative of an SNR are not correlated with the optical shell. Rather they are off-centre, protruding from the shell to the north-west. We identify the optical shell as being the HII region DEM L90 (Davies et al. 1976) which contains the stellar cluster BSDL 777 (Bica et al. 1999). Glatt et al. (2010) estimated the age of the cluster to be ~ 16 Myr. We suggest that this cluster has created and is currently photo-ionising the optical shell and that the SNR is located in projection. The SN progenitor could have been a member of BSDL 777, though it might also be possible that an older star in the locality underwent a Type Ia event.

The X-ray supernova remnant is the faintest in our sample. The emission is most prominent in the 0.7–1.1 keV band and fills the region delineated by the shell identified in the [S II]/H α image. This could suggest an Fe-rich ejecta origin though the observation is much too shallow to confirm this. We obtained some constraints on the properties of the emitting plasma by assuming it is described by a thermal plasma in CIE of LMC abundance. We used the size of the shell estimated from the [S II]/H α image with the Sedov dynamical model to determine an initial explosion energy in the range $(0.01 - 1.75) \times 10^{51}$ erg and age of 12–22 kyr. These, along with other properties, are listed in Table 8.

6 SUMMARY

We presented new XMM-Newton observations of a sample of X-ray faint SNR candidates and two previously confirmed SNRs. The main findings of our analysis on these objects can be summarised as follows:

- No X-ray emission was detected from the SNR candidate 0457–6739. Because of the lack of a clear optical shell with enhanced [S II], X-ray emission, or non-thermal radio emission, we cannot confirm this candidate as an SNR.
- Four of the SNRs, namely MCSNR J0448–6700, MCSNR J0456–6950, MCSNR J0512–6717, MCSNR J0527–7134, display X-ray morphologies and spectra that are consistent with evolved Sedov-phase remnants.
- Two SNRs, the newly confirmed MCSNR J0504–6723 and previously known MCSNR J0542–7014, were identified as members of the evolved remnants with a bright Fe-rich core (see Maggi et al. 2014; Kavanagh et al. 2016; Maggi et al. 2016, for example). This

brings the total number to 13, 18% of the confirmed LMC SNR population (see Table 9). The Fe-rich core of MCSNR J0504–6723 is surrounded by a soft X-ray shell. This remnant is unusually shaped which we suggest has been imposed by the inhomogeneous density environment into which it is evolving. MCSNR J0542–7104, which was confirmed as an SNR by Yew et al. (2021), exhibits a distinct Fe-rich core but without the soft Sedov shell. Such a morphology has previously been observed in, e.g. MCSNR J0508–6830, MCSNR J0511–6759 (Maggi et al. 2014), and MCSNR J0527–7104 (Kavanagh et al. 2016), and is interpreted as the shell evolving to the point that it is no longer visible in X-rays.

- MCSNR J0447–6919 displayed a clear optical shell with enhanced [S II] emission, with very faint emission in the interior which is elongated along its major axis. Morphologically, this is similar to MCSNR J0527–7104 in which the X-ray emission is primarily due to Fe ejecta (Kavanagh et al. 2016). Because of the faintness of the X-ray emission in MCSNR J0447–6919, we could only fit simple models to the spectrum, which do indicate a possible Fe enhancement and suggests that this object is a candidate for the evolved Fe-rich class of LMC SNRs.

- MCSNR J0449–6903 is the most unusual object in our sample, exhibiting a faint, soft shell consistent with an evolved SNR which surrounds harder emission in the core region. The core emission could be described with either thermal or non-thermal models, though the non-thermal interpretation appears more likely given the lack of abundance enhancements which would be expected from hot ejecta emission. We suggest that the hard emission could be due to a faint PWN, though there does not appear to be a correlated radio counterpart (Bozzetto et al. 2017). The true origin of the hard X-ray emission in the core remains unclear.

- MCSNR J0510–6708 appears to be located in projection with a large, circular optical shell, identified as the HII region DEM L90 (Davies et al. 1976) which is powered by BSDL 777 (Bica et al. 1999). The extent of the SNR is evident by its [S II]/H α contour with faint X-ray emission filling this shell. Our X-ray spectral analysis was severely hampered by count statistics, however, the X-ray and [S II]/H α characteristics were enough to confirm the SNR nature.

We confirmed seven of our candidates as SNRs for the first time. These add to the 64 previously known SNRs (Yew et al. 2021, and references therein) for a new total of 71 confirmed SNRs in the LMC. The upcoming new generation radio (ASKAP (Pennock et al. (2021), Bozzetto et al. in prep), MeerKAT & ATCA) and X-ray (eROSITA) surveys expects to discover even more LMC SNRs such as the LMC Odd Radio Circle J0524–6948 (Filipović et al., submitted).

ACKNOWLEDGEMENTS

This research has made use of the VizieR catalogue access tool, CDS, Strasbourg, France (DOI: 10.26093/cds/vizier).

DATA AVAILABILITY

The X-ray data used in this work are available through the XMM-Newton Science Archive (XSA): <https://www.cosmos.esa.int/web/xmm-newton/xsa>.

REFERENCES

- Acker A., Köppen J., Samland M., Stenholm B., 1989, *The Messenger*, **58**, 44
- Arnaud K. A., 1996, in Jacoby G. H., Barnes J., eds, *Astronomical Society of the Pacific Conference Series Vol. 101, Astronomical Data Analysis Software and Systems V*. p. 17
- Balucinska-Church M., McCammon D., 1992, *ApJ*, **400**, 699
- Bica E. L. D., Schmitt H. R., Dutra C. M., Oliveira H. L., 1999, *AJ*, **117**, 238
- Borkowski K. J., Lyerly W. J., Reynolds S. P., 2001, *ApJ*, **548**, 820
- Borkowski K. J., Hendrick S. P., Reynolds S. P., 2006, *ApJ*, **652**, 1259
- Bozzetto L. M., et al., 2014, *MNRAS*, **439**, 1110
- Bozzetto L. M., et al., 2017, *ApJS*, **230**, 2
- Cappellari M., Copin Y., 2003, *MNRAS*, **342**, 345
- Chen L.-W., Fabian A. C., Gendreau K. C., 1997, *MNRAS*, **285**, 449
- Childress M. J., Vogt F. P. A., Nielsen J., Sharp R. G., 2014, *Ap&SS*, **349**, 617
- Davies R. D., Elliott K. H., Meaburn J., 1976, *Mem. RAS*, **81**, 89
- Dickey J. M., Lockman F. J., 1990, *ARA&A*, **28**, 215
- Diehl S., Statler T. S., 2006, *MNRAS*, **368**, 497
- Dopita M., Hart J., McGregor P., Oates P., Bloxham G., Jones D., 2007, *Ap&SS*, **310**, 255
- Dopita M., et al., 2010, *Ap&SS*, **327**, 245
- Fazio G. G., et al., 2004, *ApJS*, **154**, 10
- Fesen R. A., Blair W. P., Kirshner R. P., 1985, *ApJ*, **292**, 29
- Filipović M. D., Tothill N. F. H., eds, 2021b, *Multimessenger Astronomy in Practice*. 2514-3433, IOP Publishing, doi:10.1088/2514-3433/ac2256, <https://dx.doi.org/10.1088/2514-3433/ac2256>
- Filipović M. D., Tothill N. F. H., 2021a, *Principles of Multimessenger Astronomy*, doi:10.1088/2514-3433/ac087e.
- Filipovic M. D., Haynes R. F., White G. L., Jones P. A., 1998, *A&AS*, **130**, 421
- Filipović M. D., et al., 2021, *MNRAS*, **507**, 2885
- Filipović M. D., et al., 2022, *MNRAS*,
- Fukui Y., et al., 2008, *ApJS*, **178**, 56
- Gaensler B. M., Hendrick S. P., Reynolds S. P., Borkowski K. J., 2003, *ApJ*, **594**, L111
- Gelfand J. D., Slane P. O., Zhang W., 2009, *ApJ*, **703**, 2051
- Glatt K., Grebel E. K., Koch A., 2010, *A&A*, **517**, A50
- Haberl F., Pietsch W., 1999, *A&AS*, **139**, 277
- Haberl F., et al., 2012, *A&A*, **543**, A154
- Hamilton A. J. S., Sarazin C. L., Chevalier R. A., 1983, *ApJS*, **51**, 115
- Hendrick S. P., Borkowski K. J., Reynolds S. P., 2003, *ApJ*, **593**, 370
- Hughes J. P., Ghavamian P., Rakowski C. E., Slane P. O., 2003, *ApJ*, **582**, L95
- Iwamoto K., Brachwitz F., Nomoto K., Kishimoto N., Umeda H., Hix W. R., Thielemann F.-K., 1999, *ApJS*, **125**, 439
- Jansen F., et al., 2001, *A&A*, **365**, L1
- Kahn F. D., 1975, *International Cosmic Ray Conference*, **11**, 3566
- Kalberla P. M. W., Burton W. B., Hartmann D., Arnal E. M., Bajaja E., Moras R., Pöppel W. G. L., 2005, *A&A*, **440**, 775
- Kavanagh P. J., Sasaki M., Bozzetto L. M., Filipović M. D., Points S. D., Maggi P., Haberl F., 2015a, *A&A*, **573**, A73
- Kavanagh P. J., Sasaki M., Whelan E. T., Maggi P., Haberl F., Bozzetto L. M., Filipović M. D., Crawford E. J., 2015b, *A&A*, **579**, A63
- Kavanagh P. J., Sasaki M., Bozzetto L. M., Points S. D., Filipović M. D., Maggi P., Haberl F., Crawford E. J., 2015c, *A&A*, **583**, A121
- Kavanagh P. J., et al., 2016, *A&A*, **586**, A4
- Kim S., Staveley-Smith L., Dopita M. A., Sault R. J., Freeman K. C., Lee Y., Chu Y.-H., 2003, *ApJS*, **148**, 473
- Kim D.-W., Protopapas P., Trichas M., Rowan-Robinson M., Khardon R., Alcock C., Byun Y.-I., 2012, *ApJ*, **747**, 107
- Kosenko D., Helder E. A., Vink J., 2010, *A&A*, **519**, A11
- Kuntz K. D., Snowden S. L., 2008, *A&A*, **478**, 575
- Kuntz K. D., Snowden S. L., 2010, *ApJS*, **188**, 46
- Maggi P., et al., 2014, *A&A*, **561**, A76
- Maggi P., et al., 2016, *A&A*, **585**, A162
- Maitra C., Haberl F., Maggi P., Kavanagh P. J., Vasilopoulos G., Sasaki M., Filipović M. D., Udalski A., 2021, *MNRAS*, **504**, 326
- Mathewson D. S., Clarke J. N., 1973, *ApJ*, **179**, 89
- Meixner M., et al., 2006, *AJ*, **132**, 2268
- Meyer D. M. A., Langer N., Mackey J., Velázquez P. F., Gusdorf A., 2015, *MNRAS*, **450**, 3080
- Nikolaev S., Drake A. J., Keller S. C., Cook K. H., Dalal N., Griest K., Welch D. L., Kanbur S. M., 2004, *ApJ*, **601**, 260
- Park T., Kashyap V. L., Siemiginowska A., van Dyk D. A., Zezas A., Heinke C., Wargelin B. J., 2006, *ApJ*, **652**, 610
- Pennock C. M., et al., 2021, *MNRAS*, **506**, 3540
- Petre R., Hwang U., Holt S. S., Safi-Harb S., Williams R. M., 2007, *ApJ*, **662**, 988
- Pietrzyński G., et al., 2013, *Nature*, **495**, 76
- Proxauf B., Öttl S., Kimeswenger S., 2014, *A&A*, **561**, A10
- Rieke G. H., et al., 2004, *ApJS*, **154**, 25
- Sasaki M., Plucinsky P. P., Gaetz T. J., Smith R. K., Edgar R. J., Slane P. O., 2004, *ApJ*, **617**, 322
- Seward F. D., Williams R. M., Chu Y. H., Dickel J. R., Smith R. C., Points S. D., 2006, *ApJ*, **640**, 327
- Shull J. M., van Steenberg M., 1982, *ApJS*, **48**, 95
- Smith R. C., Points S. D., Winkler F., 2006, *NOAO Newsletter*, **85**, 6
- Snowden S. L., Mushotzky R. F., Kuntz K. D., Davis D. S., 2008, *A&A*, **478**, 615
- Strüder L., et al., 2001, *A&A*, **365**, L18
- Sturm R. K. N., 2012, PhD thesis, Fakultät für Physik, Technische Universität München, Germany
- Turner M. J. L., et al., 2001, *A&A*, **365**, L27
- Vink J., 2012, *A&ARv*, **20**, 49
- Werner M. W., et al., 2004, *ApJS*, **154**, 1
- Williams R. M., Chu Y. H., Dickel J. R., Gruendl R. A., Seward F. D., Guerrero M. A., Hobbs G., 2005, *ApJ*, **628**, 704
- Wilms J., Allen A., McCray R., 2000, *ApJ*, **542**, 914
- Yew M., et al., 2021, *MNRAS*, **500**, 2336
- van der Marel R. P., Cioni M.-R. L., 2001, *AJ*, **122**, 1807

APPENDIX A: POINT SOURCE ANALYSIS

In this appendix we describe the methodology for the analysis and identification of point sources possibly associated with our SNR sample, followed by a brief description of each. The nature of the point sources could indicate the type of SN explosion that produced the SNRs. We follow the same procedure described in Kavanagh et al. (2015b). We assigned *XMM-Newton* identifiers to each of the sources following the source naming conventions⁸. For a detailed description of the source detection see Sect. 3.2.

We found that almost all sources were too faint for a meaningful spectral analysis. Instead, we performed a hardness ratio (HR) analysis which compares the number of counts in certain energy bands to determine the approximate shape of the spectrum, allowing spectral parameters to be inferred. The source HRs are determined using Eq. 5 of Kavanagh et al. (2015b) for the same three energy bands, i.e. $i_1 = 0.3 - 1$ keV, $i_2 = 1 - 2$ keV, and $i_3 = 2 - 4.5$ keV, using the BEHR code (ver. 12-12-2013, Park et al. 2006)⁹. We then compared our derived source HRs to synthetic HR grids which were produced from either a power law or a CIE model absorbed by material in the Galaxy and LMC (phabs*vphabs*pow and phabs*vphabs*apec in XSPEC, respectively), which allowed us to infer the source spectral parameters implied by the HR values

⁸ See <https://www.cosmos.esa.int/web/xmm-newton/source-naming-convention>

⁹ See <http://hea-www.harvard.edu/astrostat/behrr/>

(see Kavanagh et al. 2015b). These were generated by simulating a set of spectra with Galactic absorption ($N_{\text{H,Gal}}$) fixed as appropriate for each SNR, and varying values of LMC foreground absorption, and photon index (Γ) or plasma temperature (kT). The grids for each model and source HRs are shown for each of our SNRs in Figs. A1, A2, and A3.

Source variability can also provide insight into the nature of the point sources. To search for variability, we extracted light curves for each in the 0.3–10 keV range from a barycentric-corrected PN event list, correcting for instrumental effects and background using the SAS task `epi.c1ccorr`. We only considered EPIC-pn data in our variability analysis because of the higher count statistics compared to the EPIC-MOS data. We found no evidence of variability in any of our sources.

Multi-wavelength counterparts to the X-ray sources were identified by querying all catalogues on the CDS Vizier service using the Astroquery¹⁰ affiliated package of astropy. The identified counterparts are listed in Table A1.

A1 MCSNR J0447–6919

Three point sources were detected in MCSNR J0447–6919, which are listed in Table A1. XMMU J044718.1–691900 was the most centrally located source with XMMU J044700.7–691721 and XMMU J044702.7–691807 located near the northern shell (Fig. 2, top-left). The HRs for each of the sources are plotted on HR diagrams in Fig. A1, along with the HR grids.

XMMU J044718.1–691900 is located quite far from either of the grids. This is likely because its spectrum is not well described by either model used to produce the HR grids. The position of XMMU J044700.7–691721 signifies a high absorption and suggests the source is located beyond the LMC, assuming there is no local or intrinsic absorption of the source emission. A photon index $\Gamma \sim 2-3$ is inferred from the power law grid while a plasma temperature $kT \sim 2-5$ keV is inferred from the thermal grid. The spectral parameters implied by the power law grid could be consistent with an AGN. XMMU J044702.7–691807 is less affected by absorption than XMMU J044700.7–691721, and is consistent with LMC absorption in both power law and thermal plasma derived grids. A photon index $\Gamma \sim 1-2$ is inferred from the power law grid while a plasma temperature $kT \gtrsim 3$ keV is inferred from the thermal plasma grid.

An IR counterpart was found for XMMU J044718.1–691900, namely SSTITISAGEMA J044717.97–691859.7 from the *Spitzer* SAGE Survey (Meixner et al. 2006), but is of unknown source type. No counterparts were found for XMMU J044700.7–691721 or XMMU J044702.7–691807. The nature of each of these sources remains unclear.

A2 MCSNR J0448–6700

Four point sources were detected in MCSNR J0448–6700, which are listed in Table A1. All four of the sources were located close to the SNR shell (Fig. 3, top-left) and were too faint for spectral analysis. The HRs for each of the sources are plotted on HR diagrams in Fig. A1, along with the HR grids.

The location of the three sources XMMU J044804.9–670040, XMMU J044814.0–670039, XMMU J044839.2–670159 on the HR grids indicate low foreground absorptions, consistent with the LMC. A value of $\Gamma \sim 1.5$ is inferred from the power law grid while $kT \gtrsim$

10 keV is inferred from the thermal grid for XMMU J044804.9–670040. Similar values are seen for XMMU J044814.0–670039 with $\Gamma \lesssim 1.5$ and $kT \gtrsim 10$ keV inferred from the power law and thermal grids, respectively. The HRs of XMMU J044839.2–670159 suggest a softer spectrum with $\Gamma \sim 1.5-2.5$ and $kT \gtrsim 3$ keV inferred. The position of XMMU J044808.1–665857 in the HR diagram suggests the source is located beyond the LMC, assuming there is no local or intrinsic absorption of the source emission. A photon index $\Gamma \sim 2.5-4$ is inferred from the power law grid while $kT \sim 1-3$ keV is inferred from the thermal grid. The implied spectral parameters from the power law grid could be consistent with an AGN.

Counterparts were found for all of these sources. Only the counterpart of XMMU J044808.1–665857, WISEA J044807.96–665859.2, had a confirmed source type - an AGN. The nature of all sources except XMMU J044808.1–665857 remains unclear. The location of all four sources projected near the shell of the SNR suggests that they are unlikely to be the compact remnant of the explosion.

A3 MCSNR J0449–6903

Only one point source was detected in MCSNR J0449–6903, which is listed in Table A1. The source, XMMU J044922.4–690336, is located towards the western edge of the remnant (Fig. 4, top-left). Its HRs are plotted on HR diagrams in Fig. A1 along with the HR grids.

The location of the source on the HR grids indicates a low foreground absorption, consistent with the LMC. A value of $\Gamma \sim 2$ is inferred from the power law grid while $kT \gtrsim 5$ keV is inferred from the thermal grid. An IR counterpart was identified but there is insufficient information to assign a source class. Therefore its nature remains unclear.

A4 MCSNR J0456–6950

Seven point sources were detected in MCSNR J0456–6950, which are listed in Table A1. The seven sources are distributed around this large and faint SNR (Fig. 5, top-left).

The HRs for each of the sources are plotted on HR diagrams in Fig. A2 along with the HR grids. Two of the sources, XMMU J045639.7–695232 and XMMU J045651.8–695041, are located outside both the power law and thermal plasma HR grids suggesting that these models do not accurately describe their spectra. The sources XMMU J045640.4–695132, XMMU J045639.3–695026, and XMMU J045626.8–694945 are located on the power law HR grid but not on the thermal plasma grid. They are all consistent with lower absorption as expected for the LMC, with power law indices in the range $\Gamma \approx 2-4$. The location of XMMU J045622.3–695230 on both grids also indicates a low absorption and either a high photon index ($\Gamma \gtrsim 4$) or a low plasma temperature ($kT \lesssim 1$ keV).

Multi-wavelength counterparts were found for four of the seven sources (Table A1). Only the counterpart for XMMU J045639.7–695232, MACHO 17.2587.1178, had a source type classification as possible quasar. The nature of the remaining sources remains unclear.

A5 MCSNR J0504–6723

One point source was detected in MCSNR J0504–6723, which is listed in Table A1. XMMU J050500.1–672250 is located close to the north-eastern shell of the remnant (Fig. 7, top-left). The source

¹⁰ See <https://astroquery.readthedocs.io/en/latest/>

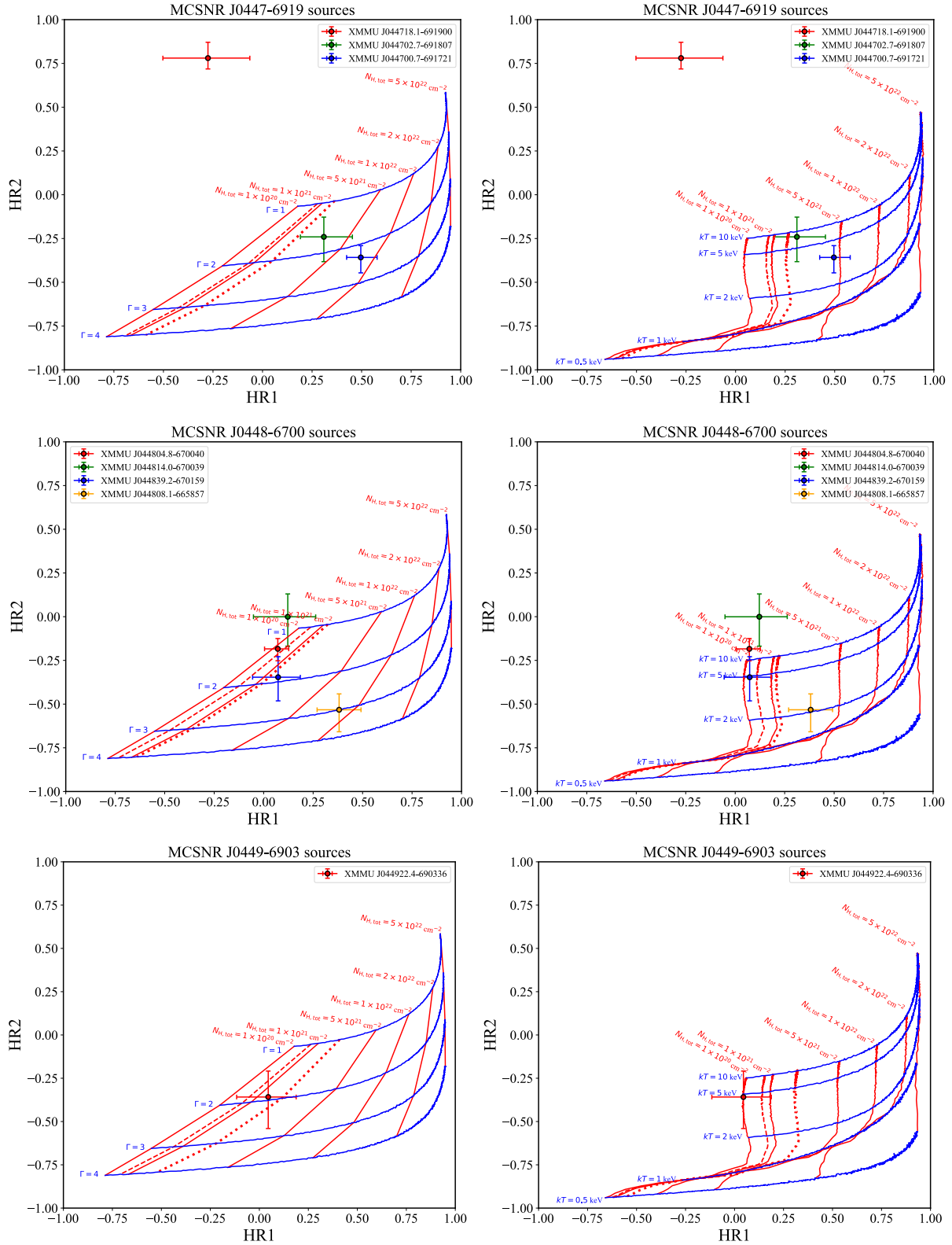


Figure A1. HR plots derived from grids of simulated absorbed power-law spectra (left) and absorbed thermal plasma (right) with the HRs from sources in MGSNR J0447–6919 (top), MGSNR J0448–6700 (middle), and MGSNR J0449–6903 (bottom). The blue lines indicate models on the grid of equal Γ (left) and kT (right), whereas the red lines mark the models on the grid of equal equivalent hydrogen column $N_{\text{H,tot}} = N_{\text{H,Gal}} + N_{\text{H,LMC}}$. The dashed red line gives the total N_{H} measured through the Galaxy and the LMC from (Kalberla et al. 2005) and the dotted red line gives the combined N_{H} measured through the Galaxy and the LMC by summing the Galactic N_{H} from Dickey & Lockman (1990) to the LMC N_{H} values from Kim et al. (2003).

Table A1. Detected point source counterparts.

No.	Name	RA (J2000)	Dec (J2000)	Counterpart	Waveband	Source type
MCSNR J0447–6919						
1	XMMU J044700.7–691721	04:47:00.7	–69:17:21	–	–	–
2	XMMU J044702.7–691807	04:47:02.7	–69:18:07	–	–	–
3	XMMU J044718.1–691900	04:47:18.1	–69:19:00	WISEA J044717.89–691859.4	IR	–
MCSNR J0448–6700						
1	XMMU J044804.9–670040	04:48:04.9	–67:00:40	WISEA J044804.82–670042.1	IR	–
2	XMMU J044808.1–665857	04:48:08.1	–66:58:57	WISEA J044807.96–665859.2	IR	AGN
3	XMMU J044814.0–670039	04:48:14.0	–67:00:39	WISEA J044814.67–670037.0	IR	–
4	XMMU J044839.2–670159	04:48:39.2	–67:01:59	WISEA J044839.16–670201.8	IR	–
MCSNR J0449–6903						
1	XMMU J044922.4–690336	04:49:22.4	–69:03:36	SSTSL2 J044922.14–690339.0	IR	–
MCSNR J0456–6950						
1	XMMU J045622.3–695230	04:56:22.3	–69:52:30	SSTSL2 J044922.14–690339.0	IR	–
2	XMMU J045623.0–695142	04:56:23.0	–69:51:42	–	–	–
3	XMMU J045626.8–694945	04:56:26.8	–69:49:45	2MASS J04562647–6949415	IR	–
4	XMMU J045639.3–695026	04:56:39.3	–69:50:26	–	–	–
5	XMMU J045639.7–695232	04:56:39.7	–69:52:32	MACHO 17.2587.1178	opt,IR	quasar cand.
6	XMMU J045640.4–695132	04:56:40.4	–69:51:32	WISEA J045640.58–695134.0	IR	–
7	XMMU J045651.8–695041	04:56:51.8	–69:50:41	–	–	–
MCSNR J0504–6723						
1	XMMU J050500.1–672250	05:05:00.1	–67:22:50	SSTSL2 J050500.52–672252.4	IR	–
MCSNR J0512–6717						
1	XMMU J051224.8–671736	05:12:24.8	–67:17:36	WISEA J051225.10–671737.1	IR	–
2	XMMU J051231.3–671754	05:12:31.3	–67:17:54	–	–	–
3	XMMU J051240.8–671720	05:12:40.8	–67:17:20	2MASS J05124058–6717225	IR,X?	HMXB?
MCSNR J0527–7134						
1	XMMU J052744.7–713354	05:27:44.7	–71:33:54	–	–	–
2	XMMU J052746.5–713305	05:27:46.5	–71:33:05	WISEA J052746.38–713303.8	opt,IR	C
MCSNR J0542–7104						
1	XMMU J054231.9–710603	05:42:31.9	–71:06:03	WISEA J054231.87–710558.6	IR	–
2	XMMU J054307.4–710409	05:43:07.4	–71:04:09	PMN J0543–7104	–	–

HRs are plotted on the HR diagrams in Fig. A2, along with the HR grids.

The location of XMMU J050500.1–672250 relative to the thermal grid suggests that this model is not a good description of the source emission. Therefore, we only discuss the power law parameters. The location of the source on the power law grid indicates a low foreground absorptions, consistent with the LMC. A value of $\Gamma \sim 1.5 - 2.5$ is inferred.

The IR source SSTSL2 J050500.52–672252.4 was identified as a counterpart to XMMU J050500.1–672250. However, the source type of the counterpart is unknown so the nature of this source remains unclear. Its location to the extreme north of the SNR suggests that it is unlikely to be the compact remnant of the explosion.

A6 MCSNR J0510–6708

No point sources were detected in MCSNR J0510–6708

A7 MCSNR J0512–6717

Three point sources were detected in MCSNR J0512–6717 located to the south and southeast of the centre. XMMU J051224.8–671736 and XMMU J051231.3–671754 are located interior to the soft X-ray shell while XMMU J051240.8–671720 is embedded in the eastern shell.

The source HRs are plotted on the HR diagrams in Fig. A3, along with the HR grids. The position of XMMU J051224.8–671736 on

both grids indicates a high N_H with a location beyond the LMC. The HRs point to a $\Gamma < 2$ or $kT > 5$ keV, both signifying a hard source and a possible AGN, though this cannot be confirmed with the available data. The location of XMMU J051231.3–671754 off both the thermal and power law grids suggests that neither model is representative of the source spectrum. XMMU J051240.8–671720 is located off the power law grid but its position on the thermal plasma grid suggests a soft thermal source with the absorption consistent with the LMC.

Two of the sources, XMMU J051224.8–671736 and XMMU J051240.8–671720, were correlated with IR counterparts (see Table A1), however neither counterpart has a confirmed source type. Interestingly, XMMU J051240.8–671720 is also a possible counterpart to the high-mass X-ray binary RX J0512.6–6717 (Haberl & Pietsch 1999) identified with ROSAT, though its location in the shell suggests it is unlikely to be related to the supernova explosion. No counterpart was identified for XMMU J051231.3–671754.

A8 MCSNR J0527–7134

Two point sources were detected in MCSNR J0527–7134, XMMU J052744.7–713354 to the north and XMMU J052746.5–713305 slightly west of the SNR centre. The source HRs are plotted on the HR diagrams in Fig. A3, along with the HR grids. The position of XMMU J052744.7–713354 and XMMU J052746.5–713305 on the power law grid indicates a high N_H with a location beyond the

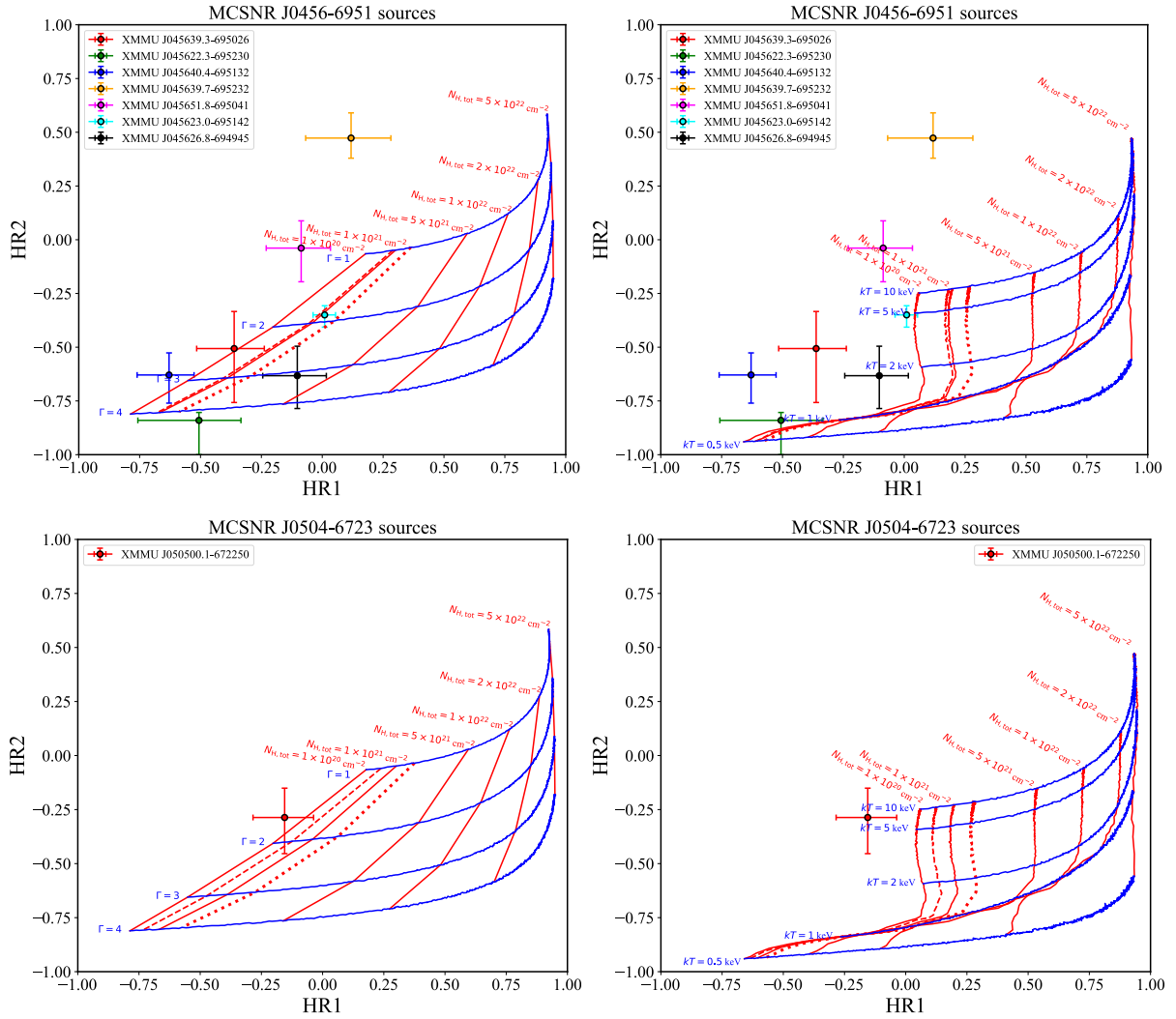


Figure A2. Same as Fig. A1 but for MCSNR J0456–6950 (top), MCSNR J0504–6723 (bottom).

LMC and a $\Gamma = 1.5 - 2.52$. However, their location on the thermal plasma grid suggests a lower foreground absorption consistent with the LMC and $kT > 2$ keV.

We searched for multi-wavelength counterparts to these sources which are listed in Table A1. XMMU J052746.5–713305 was the only source with a counterpart, identified as MACHO 21.7644.561 and is a quasar candidate (Kim et al. 2012). Therefore, it is likely unrelated to MCSNR J0527–7134. No counterpart was identified for XMMU J052744.7–713354. Its location slightly offset from the SNR centre to the west suggests that it could potentially be the compact remnant of the explosion, though its nature remains unclear.

A9 MCSNR J0542–7104

Two point sources were detected in MCSNR J0542–7104, XMMU J054231.9–710603 to the south and XMMU J054307.4–710409 to the east. Both sources are quite faint and located at the extremities of the SNR shell, already suggesting that they are not the compact remnants of the explosion. The source HRs are plotted on the HR diagrams in Fig. A3, along with the HR grids. Neither source is located on the thermal plasma grid indicating that

this model is not a good description of the source emission. Only XMMU J054231.9–710603 is located on the power law grid, with its location suggesting an absorption consistent with the LMC and a hard spectrum with Γ 1.

We searched for multi-wavelength counterparts to these sources which are listed in Table A1. XMMU J054231.9–710603 is correlated with an IR source and a radio source but no source classification exists for either.

This paper has been typeset from a $\text{\TeX}/\text{\LaTeX}$ file prepared by the author.

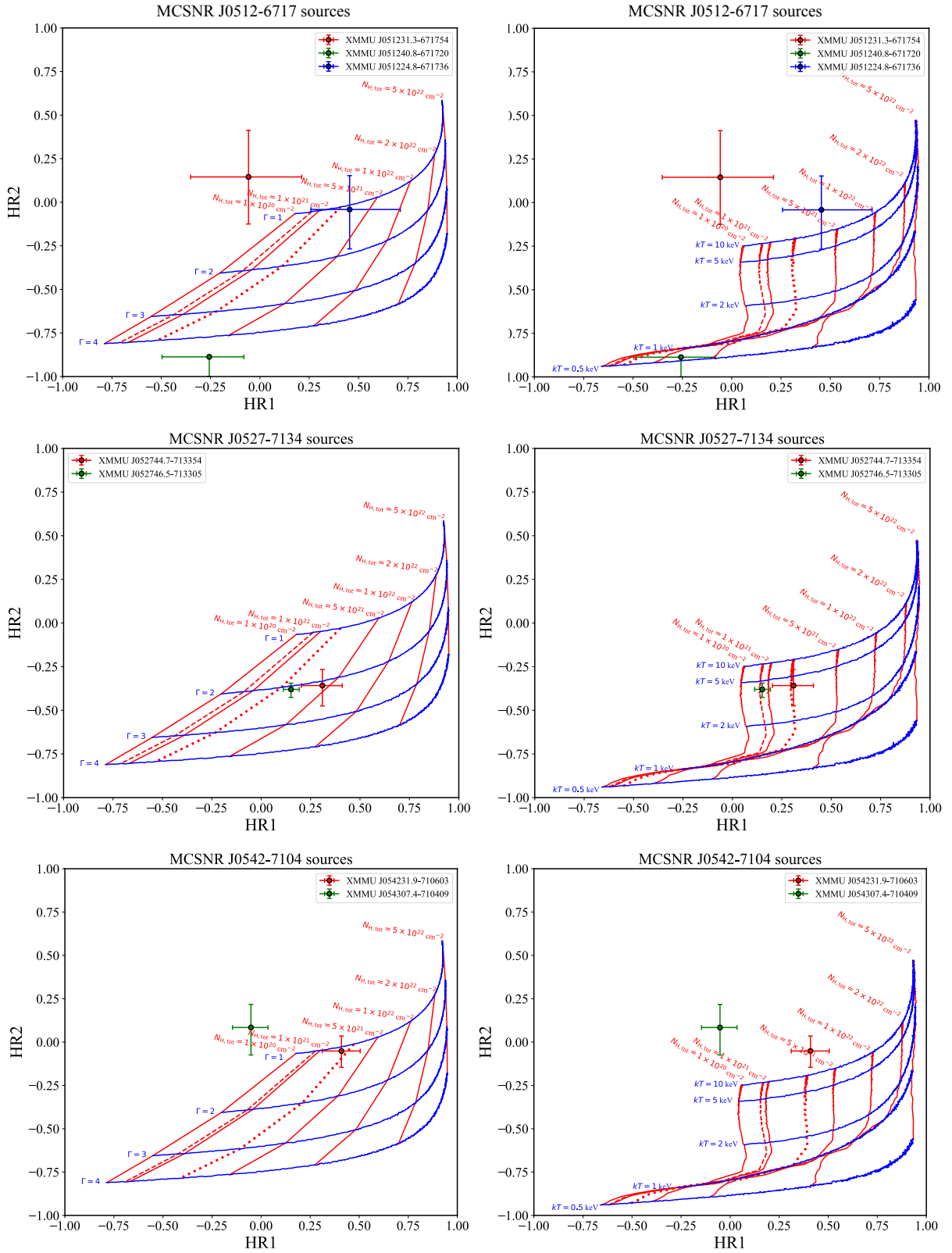


Figure A3. Same as Fig. A1 but for MCSNR J0512–6717 (top), MCSNR J0527–7134 (middle), and MCSNR J0542–7104 (bottom).